



Open Archive Toulouse Archive Ouverte (OATAO)

OATAO is an open access repository that collects the work of Toulouse researchers and makes it freely available over the web where possible

This is an author's version published in: <http://oatao.univ-toulouse.fr/26627>

Official URL: <https://doi.org/10.1016/j.corsci.2020.108684>

To cite this version: Sanviemvongsak, Tom and Monceau, Daniel and Desgranges, Clara and Macquaire, Bruno *Intergranular oxidation of Ni-base alloy 718 with a focus on additive manufacturing*. (2020) Corrosion Science, 170. 108684. ISSN 0010938X

Any correspondence concerning this service should be sent to the repository administrator: tech-oatao@listes-diff.inp-toulouse.fr

Intergranular oxidation of Ni-base alloy 718 with a focus on additive manufacturing

Tom Sanviemvongsak^{a,b,*}, Daniel Monceau^a, Clara Desgranges^b, Bruno Macquaire^b

^a CIRIMAT, Université De Toulouse, CNRS, INPT, ENSIACET, 4 Allée Emile Monso, BP 44362, 31030, Toulouse Cedex 4, France

^b Safran Paris-Saclay, Safran Tech, Rue Des Jeunes Bois, Châteaufort, CS 80112, 78772, Magny-Les-Hameaux, France

ARTICLE INFO

Keywords:

Superalloys
Laser beam melting
Electron beam melting
Grain boundaries oxidation
Thermocalc
Diffusion

ABSTRACT

The intergranular oxidation in air at 850 °C of alloy 718 produced by laser beam melting and electron beam melting was compared to that of the wrought alloy. Quantitative analyses revealed that the amount of grain boundary oxidation was similar for these alloys. However, the additively manufactured ones presented deeper and thicker oxides at grain boundaries, due to grain size heterogeneity and to a smaller number of special boundaries. Results show that intergranular oxidation kinetics follows Wagner's theory on internal oxidation considering not only O diffusion at the intergranular oxide/metal interfaces but also Al and Ti diffusion in the bulk.

1. Introduction

1.1. Review of intergranular oxidation of alloy Ni-base alloys

Alloy 718 (UNS N07718) is extensively used in aeronautical and nuclear applications because of its good mechanical properties at high temperature and its high-temperature oxidation resistance. Up to 650 °C, the oxidation of the polycrystalline alloy 718 may not be a problem in terms of metal consumption but this alloy is susceptible to intergranular oxidation which can cause premature mechanical failure after a long term exposure. This is the case even at lower temperatures in nuclear applications. The increase in efficiency of aircraft turbines is partly due to an increase in operating temperatures. Higher temperatures lead to an increase in oxidation kinetics, and intergranular oxidation becomes noticeable, as seen previously at 850 °C [1–3]. This form of oxidation is known to induce intergranular embrittlement and provoke intergranular fatigue crack propagation [4–8]. Al, Ti and Nb are used as alloying elements to harden the material by precipitation of γ' , γ'' and δ phases. These elements have a high affinity with oxygen which can lead to grain boundary oxidation (GBO) at very low oxygen content below the chromia oxide scale. Accordingly aluminium oxide α -Al₂O₃ [1,9] and titanium oxide rutile-TiO₂ [3] were found in the grain boundaries (GB) of alloy 718.

It is well established that alloy's GBs are preferential pathways for the diffusion of alloying elements as well as oxygen. The O diffusion coefficient in the bulk of pure nickel has been determined elsewhere

[10]. Two other studies investigated the penetration depth of O through grain boundaries. The O was found to react with carbon in the metal to form gas bubbles. The estimated activation energy for this reaction is close to 280 kJ/mol [11,12]. A recent study carried out on Fe-0.5 % Si, showed that the O diffusion coefficient along GBs, determined using Wagner's theory, could be 60–70 times higher than through the bulk [13]. In this latter study, the intergranular oxidation kinetics was supposed to be controlled only by the diffusion of O through the GBs. But when intergranular oxidation occurs, O may diffuse through metal/intergranular oxide interfaces. When dealing with internal oxidation kinetics in Ni-Al alloys, Stott *et al.* determined that O diffusion at Ni/Al₂O₃ incoherent interfaces was several orders of magnitude faster than in the bulk at 1050–1100 °C [14].

Preferential intergranular oxidation has already been studied in model alloys such as Ni-Cr [15,16] or Ni-Al [17,18]. Four types of intergranular oxidation were described by Shida *et al.* in Ni-Al alloys [17]. These authors showed that several types of morphologies could be observed depending on Al concentration and oxidation temperature. It was shown that the depth of intergranular oxides decreased by increasing Cr concentration in Ni-Cr alloys with small Cr content (Ni-1 to 5 wt. % Cr), in agreement with Wagner's theory on internal oxidation [16]. For Ni-Cr-Al model alloys, three different oxidation mechanisms were identified [19]. The first one concerns Ni-Cr-Al alloys containing a small amount of Cr (5 wt. % Cr) and Al (inferior to 3 wt. % Al), for which the external NiO scale is supplemented by internally oxidised Cr and Al. The second case concerns alloys with a large amount of Cr

* Corresponding author at: CIRIMAT, Université de Toulouse, CNRS, Toulouse INP, ENSIACET, 4 allée Emile Monso, BP 44362, 31 030, Toulouse Cedex 4, France.
E-mail address: tom.sanviemvongsak@ensiacet.fr (T. Sanviemvongsak).

(20–30 wt. % Cr) and a relatively low Al content (2 wt. % Al). These alloys, present a Cr_2O_3 -external scale and an Al_2O_3 oxide in the sub-scale, particularly concentrated at grain boundaries. This latter mechanism is typically the one found in alloy 718. Lastly, the third case concerns alloys with high Al content (4–9 wt. % Al) forming a thin and dense Al_2O_3 -external scale with no internal or intergranular oxidation [19]. Moreover, in certain cases, voids were found near the oxides formed at grain boundaries and within the bulk inside the Cr-depleted zone, for long-duration oxidation of Ni-15.1Cr-1.1Al and Ni-28.8Cr-1.0Al at 1000 °C and 1200 °C [20]. The formation of these voids was attributed to a Kirkendall effect, as seen in other studies on Ni-Cr alloys [15,21,22].

In order to increase the durability of aircraft turbines and pressurised reactor components, increasing the resistance of grain boundaries to oxidation, thereby reducing mechanical stress and fatigue in oxidising environments, should be assessed [23,24]. A study on the impact of grain size on high temperature oxidation was carried out on Cr steels [25]. This study revealed that increasing the grain size on low-Cr steels (2.25 wt. % Cr) improved oxidation resistance in terms of mass change and limited the growth of the inner oxide, especially during the transient stage. Indeed, by increasing the grain size, the volume fraction of short-circuits for the diffusion of O along GB is reduced. Conversely, for high-Cr steels (18 wt. % Cr), the combination of a high Cr content with a high fraction of diffusion short-circuits such as grain boundaries, favours the fast diffusion of Cr and the formation of a dense and protective chromia scale. This result was also found in alumina-forming alloys [26].

1.2. Specific features for alloy 718 fabricated by additive manufacturing

While studying alloy 718 fabricated by additive manufacturing, the specific microstructure should be considered as well as its consequences on intergranular oxidation. It has been shown that porous materials fabricated with unoptimised parameters suffered from large internal oxidation attacks leading to a large mass gain during oxidation tests [2]. But even dense alloys show microstructural specificities that can influence intergranular oxidation kinetics [3]. Indeed, the building direction of AM samples (the vertical direction Z, perpendicular to the powder bed) was found to impact grain boundary density and consequently the oxidation resistance of alloy 718 produced by EBM [27]. Indeed, numerous studies showed that special grain boundaries and particularly $\Sigma 3$ -boundaries, presented a higher resistance to intergranular oxidation [28–30]. Trindade *et al.* [8,9] showed that repeated thermomechanical processing increased the fraction of special grain boundaries, especially of $\Sigma 3$ -boundaries, up to 35 %. They showed that samples with a high fraction of special boundaries had better oxidation resistance in terms of mass gain but also in terms of intergranular oxidation depth.

1.3. Intergranular oxidation of additively manufactured alloy 718

None of the previously cited articles studied the intergranular oxidation resistance of additively manufactured samples and compared it to the intergranular attack of wrought material. Our first study focused on the difference in oxidation kinetics between an LBM-718 alloy, an EBM-718 alloy and a conventionally-wrought heat-treated alloy 718 [3]. Results showed similarities regarding oxidation resistance and oxide scale nature, but dissimilarities regarding GBO.

Therefore, the present paper focuses on the differences in intergranular oxidation resistance of the cited alloys oxidised at 850 °C for up to 3000 h. First, a quantification of intergranular oxidation kinetics will be presented and compared to literature data regarding wrought or additively manufactured alloys. Then, a characterisation of the microstructure, focused on grain size, misorientation and nature of GBs will be performed. The impact of grain size and grain boundary nature on GBO will be discussed. Finally, through a WDS analysis and a literature

review on diffusion coefficients, the mechanism of intergranular oxidation will be discussed.

2. Materials and experimental procedures

2.1. Additive manufacturing of alloy 718

The alloys 718 studied in the present paper were produced using two different powder bed fusion processes : laser beam melting (LBM) and electron beam melting (EBM). They were produced with the machine manufacturer's standard settings, respectively EOS™ and ARCAM™, and were studied in their as-built form, without heat-treatment. They were compared to the heat-treated wrought (WRG) alloy 718 (AMS 5662). A more detailed description of these alloys can be found in a previous paper [3], which contains the characterization of their chemical composition, their microstructure and the description of the AM parameters used to build these samples.

2.2. High temperature oxidation experiments

Samples were prepared for 48-h, 1000-h and 3000-h isothermal oxidation tests. Their dimensions approached $15 \times 10 \times 2 \text{ mm}^3$ and all sample surfaces were ground using P600-SiC paper. The grinding depth needed to remove the initial roughness was lower than 100 μm for the raw LBM sample and lower than 500 μm deep for the EBM raw sample. Samples were ultrasonically cleaned in acetone and ethanol, then dried before oxidation testing.

The three different alloys, LBM, EBM and wrought, were tested at 850 °C in a SETARAM™ TAG 24 S thermobalance with $\pm 0.1 \mu\text{g}$ sensitivity, for the 48-h oxidation test under flowing synthetic air (5 mL min^{-1}) in a reaction tube of diameter 14 mm.

The 1000-h and 3000-h oxidation tests were carried out in a box furnace in still laboratory air and weighed with a Sartorius ME215 P balance with $\pm 20 \mu\text{g}$ sensitivity.

2.3. Characterisation of oxidized samples

External oxide scale characterisation was carried out by means of X-ray diffraction conducted with a 10°-incidence mode, with a Bruker™ D8 ($k_\alpha = 1.5418 \text{ \AA}$), and scanning electron microscopy (SEM LEO435VP) equipped with an energy dispersive X-ray spectroscopy detector (EDS PGT IMIX-Ge). The cross-sections of oxidised samples were analysed using SEM.

The quantification of external oxide scale thickness and of intergranular oxidation was carried out using Image J software. External scale thickness was calculated as follows: the surface area of the external oxide scale was measured with image analysis, and the result was divided by the length of the oxide scale on the cross section (about 500–800 μm). Intergranular oxide areas were quantified on 30–50 grain boundaries for each sample. Five micrographs, with a dimension of $50 \times 35 \mu\text{m}^2$ for the 48-h and 1000-h test samples, and a dimension of $100 \times 70 \mu\text{m}^2$ for the 3000-h test samples, were taken on each sample and analysed. The grain orientation and the chemical nature of oxides at grain boundaries were identified using a scanning electron microscope (JEOL JSM-7100TTLS LV) equipped with an EDS detector (X-Max, Oxford Instruments) and an EBSD camera (NordlysNano, Oxford Instruments). The chemical composition and the elements' concentration profiles were measured using an electron probe microanalyser (EPMA SX Five FE CAMECA) calibrated on standards at 7 kV and 20 nA.

The chemical composition of the three alloys 718 is reported in Table 1. It can be noticed that the three alloys have almost the same chemical composition. For this paper, it is important to focus on the content of Al, which can react with O in the grain boundaries, and the content of Nb, which can be present in the grain boundaries as δ -phase precipitates.

Table 1
Quantitative WDS and EDS analyses of the chemical composition of tested alloy 718 samples.

		Ni	Cr	Fe	Al	Ti	Nb	Mo	O	Al + Ti
LBM (WDS)	wt.%	50.4 ± 0.9	20.1 ± 0.9	19.2 ± 0.2	0.4 ± 0.0	1.0 ± 0.1	5.0 ± 0.4	2.9 ± 0.3	–	–
	at.%	49.8 ± 0.8	21.7 ± 1.0	21.4 ± 0.2	0.9 ± 0.1	1.3 ± 0.1	3.1 ± 0.2	1.7 ± 0.2	–	2.2
EBM (WDS)	wt.%	49.8 ± 0.8	21.3 ± 0.2	19.4 ± 0.5	0.5 ± 0.0	1.1 ± 0.0	5.0 ± 0.7	2.9 ± 0.3	–	–
	at.%	49.1 ± 0.8	22.1 ± 0.3	21.6 ± 0.5	1.0 ± 0.1	1.3 ± 0.1	3.2 ± 0.4	1.8 ± 0.2	–	2.3
Wrought (WDS)	wt.%	52.7 ± 2.4	20.4 ± 0.7	18.3 ± 0.8	0.4 ± 0.0	0.9 ± 0.2	4.6 ± 0.4	2.7 ± 0.2	–	–
	at.%	52.0 ± 2.3	21.1 ± 0.8	20.4 ± 0.8	0.9 ± 0.0	1.0 ± 0.3	2.9 ± 0.2	1.6 ± 0.1	–	1.9
LBM beneath the oxide scale (EDS)	wt.%	52.7	9.5	19.8	3.0	1.2	5.7	3.7	4.3	–
	at.%	46.2	9.4	18.3	5.7	1.4	3.1	2.0	13.9	7.1

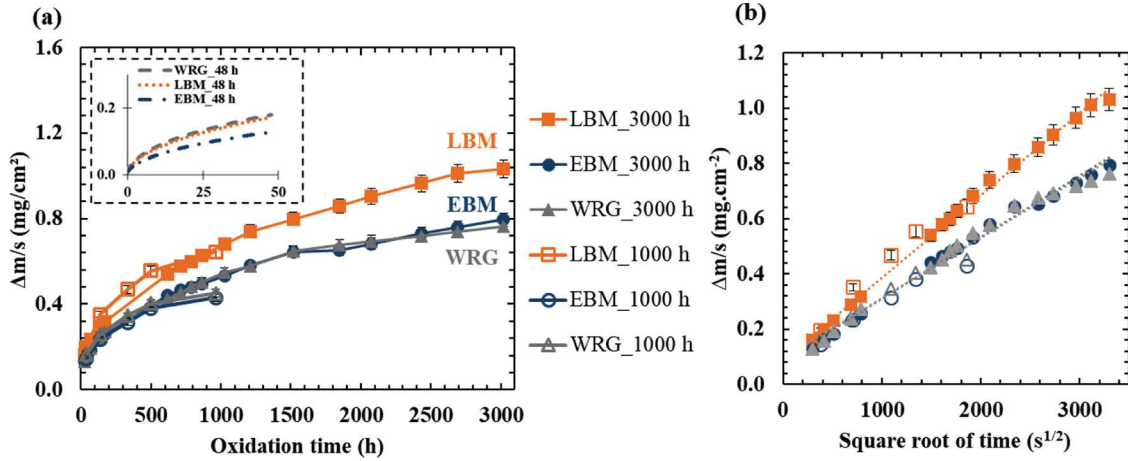


Fig. 1. (a) Isothermal oxidation kinetics and (b) apparent parabolic oxidation rate fitting of three alloys 718 (LBM, EBM, wrought) P600-ground and oxidised at 850 °C for 48 h, 1000 h and 3000 h (48 h experiments were conducted in TGA under synthetic air flow, the others in static lab air).

3. Results and discussions

3.1. Isothermal air oxidation kinetics and external/internal scale characterisation

3.1.1. Oxidation kinetics

Fig. 1(a) shows the mass variations per unit area $\Delta m/S$ (mg cm^{-2}) as a function of time of the three alloys 718. The overall relative error on the mass gain per surface area is lower than 4%. Results show that the mass gain of LBM samples (1 mg cm^{-2}) is 25% higher than that of EBM and wrought samples (0.7 mg cm^{-2}). The oxidation rate shift occurs during the transient stage, whereas during the stationary stage, when the protective chromia scale was well established, the three samples had similar oxidation rates. All samples presented a relatively low mass gain, less than 1.2 mg cm^{-2} after 3000 h of air oxidation, which corresponds to an oxide scale thickness of approximately $7 \mu\text{m}$ if we assume that most of the mass gain is due to the formation of an external scale made of chromia. In Fig. 1(b), regardless of the manufacturing process, all oxidation curves follow parabolic kinetics. Only a very slight decrease in the slopes can be observed on the parabolic plots after 2500^2 s (i.e. 1700 h) for wrought and EBM alloys. Parabolic rate constants, k_p , were determined by plotting mass gains versus square root of time [31] over 3000 h, using the following Eq. (1)

$$\frac{\Delta m}{s} = \sqrt{k_p \cdot t} + C \quad (1)$$

Where C is a constant depending on the transient stage of oxidation.

k_p values determined from 48-h to 3000-h oxidation tests are shown in Table 2. These values were quite similar, ranging from 0.4×10^{-7} to $1.8 \times 10^{-7} \text{ mg}^2 \text{ cm}^{-4} \text{ s}^{-1}$ and were similar to those previously found [3]. The maximum overall error made on the determination of k_p reached 8%. After long oxidation tests (1000 h and 3000 h), LBM samples showed an estimated k_p value 20–30% higher than those found

for EBM and wrought samples. This result is consistent with the mass gain differences. In a word, the three alloy 718 samples presented a good oxidation resistance and EBM and wrought samples presented slightly slower oxidation rates compared to LBM samples.

3.1.2. Oxide scale and cross-section analyses

The nature of the oxide scale was determined by combining XRD and EDS analyses. Fig. 2 shows the diffraction diagrams of a 718 LBM sample oxidised at 850 °C in air for 3000 h. The diffraction diagrams were taken with a X-ray source setting with a low and constant incidence angle of 10° in order to better reveal the oxide scale nature. Results show that the oxide layer of the three alloys is mainly composed of Cr_2O_3 ($a, b = 4.96 \text{ \AA}$, $c = 13.60 \text{ \AA}$, R-3cH), with small amounts of rutile- TiO_2 ($a, b = 4.59 \text{ \AA}$, $c = 2.96 \text{ \AA}$, P42/mnm), $\alpha\text{-Al}_2\text{O}_3$ ($a, b = 4.76 \text{ \AA}$, $c = 13.0 \text{ \AA}$, R-3cH) and spinel ($a, b, c = 8.44 \text{ \AA}$, Fd-3mS). In addition, some X-ray peaks of the δ phase ($a = 5.11 \text{ \AA}$, $b = 4.25 \text{ \AA}$, $c = 4.54 \text{ \AA}$, PmmnS) are also identified, especially in EBM and wrought samples. As seen in a previous paper [3], XRD peaks for Al_2O_3 and TiO_2 are certainly due to grain boundary oxidation (GBO). Enrichment in Nb was observed below the metal/oxide interface. But no δ -phase peaks were observed in the X-ray diffraction diagram of the LBM sample. Then, the cross-section of the three samples were analysed by SEM-EDS, WDS and EBSD. Fig. 3 shows SEM-BSE micrographs of the cross-section of oxidised LBM, EBM and wrought samples. All samples showed a thick and dense external oxide scale identified as a Cr_2O_3 scale. Beneath the oxide scale, at the metal/oxide interface, EBSD analysis revealed a thin layer of δ phase on all three materials.

3.1.3. Grain boundary oxidation

GBO was observed as seen previously in [3], and oxides in the GB were identified as TiO_2 and Al_2O_3 using EBSD. The most stable oxide for a metal activity of 1 is Al_2O_3 , and it was found deeper in the grain boundaries, beneath the TiO_2 . Some of the GBO penetrations appeared

Table 2

Parabolic rate constant k_p , k_p' , k_{pGBO} and $k_{pGBOmax}$ of air oxidation tests carried out at 850 °C for 48 h, 1000 h and 3000 h, all samples were ground using P600-SiC paper.

Test conditions at 850 °C		Process	Mass gain (mg cm ⁻²)	k_p (mg ² cm ⁻⁴ s ⁻¹) Equation (1) ($\times 10^{-7}$)	Oxide scale thickness (μ m)	k_p' (μ m ² s ⁻¹) k_p ($\times 10^{-6}$)	GBO Average depth (μ m)	k_{pGBO} (μ m ² h ⁻¹) Equation (2) ($\times 10^{-2}$)	GBO Maximum depth (μ m)	$k_{pGBOmax}$ (μ m ² h ⁻¹) Equation (2) ($\times 10^{-2}$)
TGA or Furnace	Time (h)									
TGA	48	LBM	0.16 ± 0.01	1.7 ± 0.27	1.0 ± 0.2	5.7 ± 0.97	3.0 ± 1.4	19 ± 3.2	4.4	40
TGA	48	EBM	0.12 ± 0.01	1.0 ± 0.16	0.7 ± 0.2	4.0 ± 0.68	2.4 ± 1.4	12 ± 2.0	2.8	27
TGA	48	WRG	0.17 ± 0.01	1.8 ± 0.29	0.6 ± 0.1	3.4 ± 0.58	2.3 ± 1.2	11 ± 1.9	3.9	32
Furnace	1000	LBM	0.61 ± 0.02	1.0 ± 0.16	3.7 ± 0.1	1.0 ± 0.17	8.7 ± 6.2	7.6 ± 1.3	14.2	20
Furnace	1000	EBM	0.44 ± 0.02	0.4 ± 0.02	2.6 ± 0.2	0.72 ± 0.12	7.9 ± 5.2	6.2 ± 1.1	12.3	15
Furnace	1000	WRG	0.45 ± 0.02	0.4 ± 0.02	3.4 ± 0.6	0.94 ± 0.16	8.6 ± 2.8	7.3 ± 1.2	11.2	13
Furnace	3000	LBM	1.03 ± 0.04	1.1 ± 0.18	7.7 ± 0.2	0.71 ± 0.12	17.7 ± 10.2	10 ± 1.7	33.9	29
Furnace	3000	EBM	0.79 ± 0.03	0.7 ± 0.11	6.9 ± 0.6	0.63 ± 0.11	18.2 ± 12.2	11 ± 1.9	35.4	34
Furnace	3000	WRG	0.76 ± 0.03	0.7 ± 0.11	7.0 ± 0.7	0.65 ± 0.11	18.6 ± 4.0	11 ± 1.9	19.4	16

deeper in AM samples than in the wrought sample. Thicker oxide at the GB was also found in AM samples.

3.1.4. Nb-rich oxide in the external oxide scale

The EPMA-WDS analysis presented in Fig. 4 confirmed the presence of Al and Ti-rich oxides at the GB, but also showed the presence of a (Ti,Nb)-rich oxide in the scale close to the metal oxide interface. This oxide was identified as TiNbO₄ by combining WDS and EBSD analyses. TiNbO₄ has a rutile-type structure (a, b = 4.74 Å, c = 3.0 Å, P42/mmm). The oxidation of the metal produces a thin Nb-rich layer at the metal/oxide interface. This layer can be observed in 48-h tests and thickens as oxidation time increases. It can still be observed in 1000-h tests, and for such durations Nb remains unoxidised. In samples oxidised for 3000 h however, the Nb is oxidised locally; TiNbO₄ was indeed detected. In previous studies, a small amount of FeNbO₄ was found in alloy 718 after 1 h at 1000 °C [33]. NbO was also found after 100-h oxidation tests at the same temperature [27]. However, this last result was not confirmed by XRD analyses, and by referring to their EDS element maps, it does not seem that the Nb was oxidised. Nb₂O₅ oxides were found on alloy 718 oxidised at 650 °C for 1000 h [34]. In addition, another work on alloy 625 [35] showed that above 1100 °C, the δ phase present beneath the oxide scale oxidised and formed NbCrO₄, another oxide with a rutile-type structure.

3.1.5. Thermodynamic calculations on the relative stability of the different oxides

As several oxides were observed in the oxide scale and in the grain boundaries underneath, a thermodynamic analysis was performed in order to evaluate whether obtained results were in agreement with local equilibrium. These calculations were performed with Thermocalc™ software using the TCNi9 Ni-database. First, a calculation of the volume fraction of phases at equilibrium at 850 °C was done as a function of O content (i.e. as a function of oxygen chemical potential or of oxygen partial pressure). This kind of calculation does not represent the actual oxygen gradient across the real system, because it is performed with the composition of the alloy and does not take into account the diffusion of the alloying elements. It is only carried out to check the relative stability of the oxides, i.e. to improve upon the information that would provide a simple Ellingham diagram in which the activity of the metallic elements and the oxide phases is assumed to be 1. For this first calculation, we used the composition of the LBM-718 alloy given in Table 1. The simulation was also conducted using the chemical composition of the wrought sample. However, this had little influence on the phases determined at the equilibrium, when compared to the AM material, therefore this last result is not shown. The result of this first calculation is given in Fig. 5. This graph gives the most stable phases that can be formed in an alloy having the composition of alloy 718, as a function of O content. It is useful to find out which are the most stable oxides in contact with the metal by taking into account the chemical activity of the metallic elements in the alloy. Indeed, since the

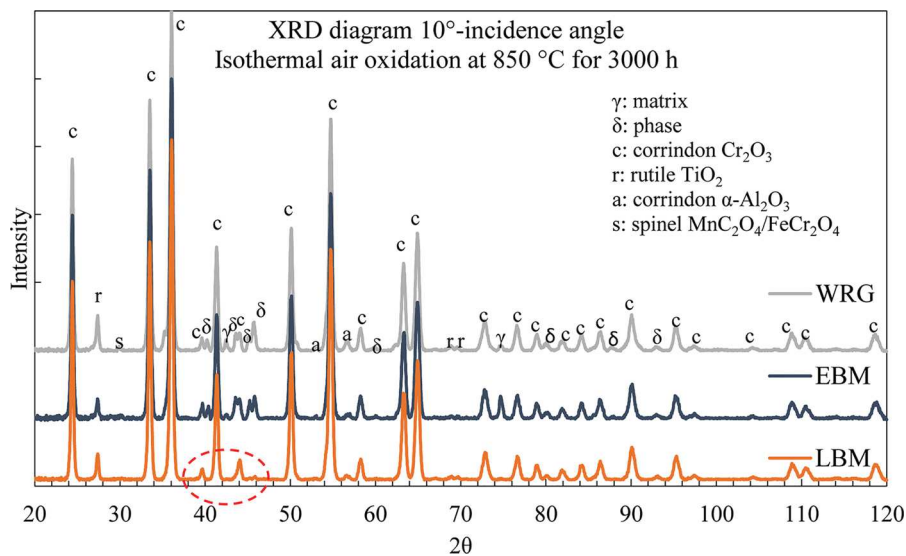


Fig. 2. X-ray diffraction diagrams of an LBM sample oxidised at 850 °C in air for 3000 h with P600-ground surface.

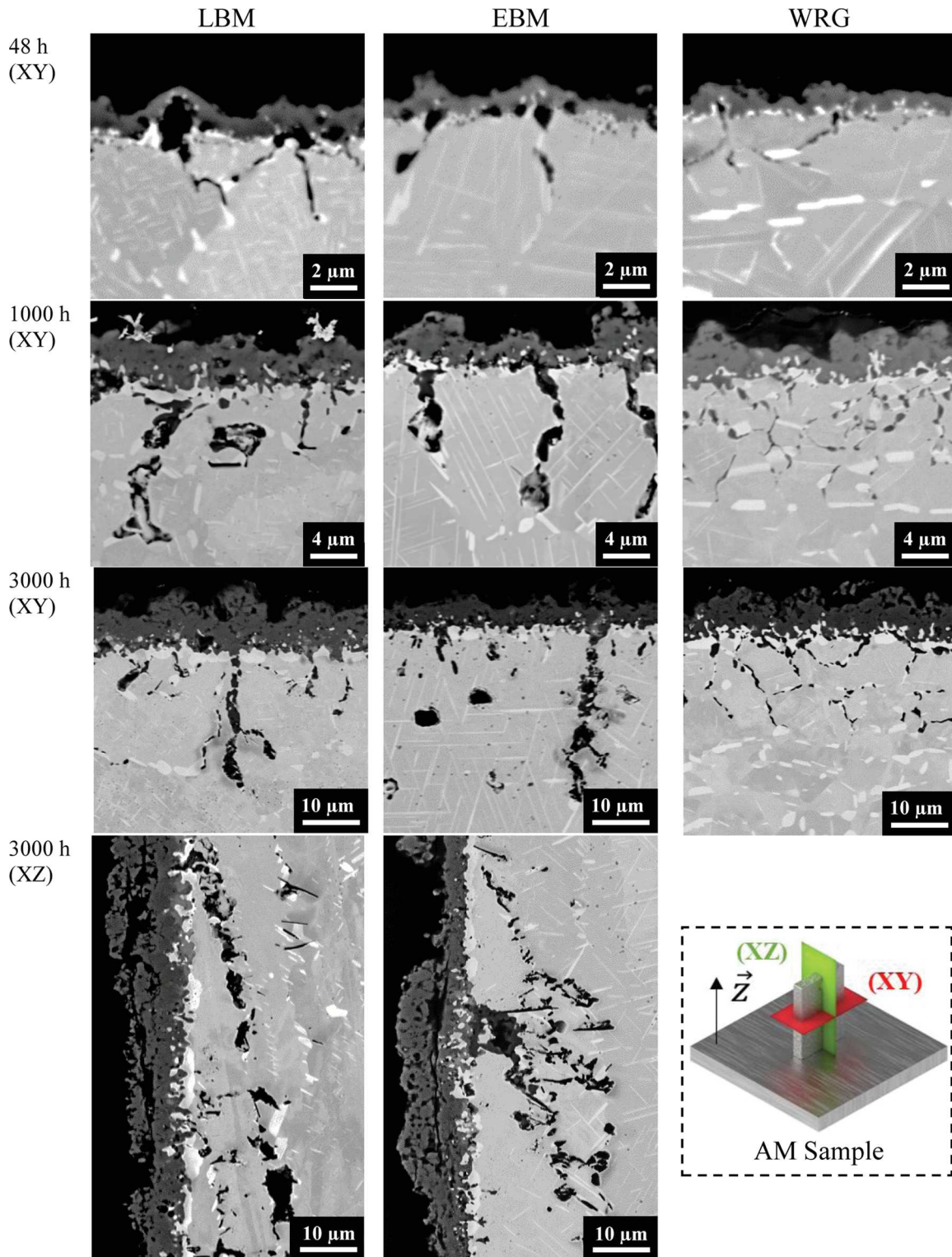
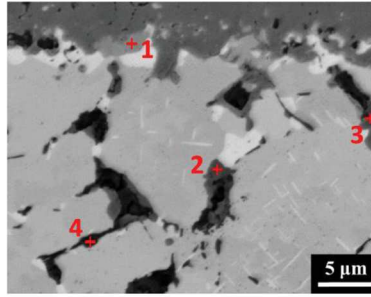


Fig. 3. SEM-BSE micrographs of the cross-section of oxidised LBM, EBM and wrought samples all ground with P600 SiC paper, oxidised for 48 h in synthetic air or for 1000 h and 3000 h in static lab air.

concentrations of Ti and Al are very low in the alloy, a calculation is necessary to know if Al_2O_3 and TiO_2 are more stable than Cr_2O_3 on alloy 718. For very low O partial pressures (below 10^{-33} atm), Fig. 5(a) shows the equilibrium phases in alloy 718 at 850 °C, with 6 % of sigma phase, 15 % of delta phase and two other phases under 1 vol. %, namely phase 3, which corresponds to (Nb,Ti)C, and phase 2, to TiCN. For P_{O_2} superior to 10^{-33} atm, the first stable oxide is corundum Al_2O_3 . This

agrees with the fact that Al_2O_3 was observed deeper in the grain boundaries, where O activity is the lowest. The second stable oxide is TiO with some Cr in solid solution. Here again, this is in agreement with the observation of a Ti-rich oxide in the grain boundaries less deep than the alumina, despite the fact that thermodynamics predicted TiO whereas diffraction (EBSD) revealed TiO_2 . The third oxide is corundum Cr_2O_3 in agreement with the formation of a chromia oxide scale on the



		O	Al	Ti	Nb	Cr	Fe	Mo	Ni	Total	Comments
1	wt.%	32.5	0.1	17.4	45.1	5.9	0.0	0.0	0.0	101.0	Nb, Ti, Cr oxide
	at.%	67.8	0.1	12.1	16.2	3.8	0.0	0.0	0.0	100.0	
2	wt.%	37.1	3.0	56.0	0.9	2.5	0.0	0.3	1.1	101.0	Ti oxide
	at.%	63.1	3.0	31.8	0.3	1.3	0.0	0.1	0.5	100.0	
3	wt.%	38.8	11.0	37.2	3.7	9.7	0.0	0.0	0.0	100.4	Ti, Al oxide
	at.%	63.2	10.6	20.3	1.0	4.9	0.0	0.0	0.0	100.0	
4	wt.%	46.8	48.5	0.4	0.7	0.7	0.0	0.1	0.0	97.1	Al oxide
	at.%	61.5	37.8	0.2	0.2	0.3	0.0	0.0	0.0	100.0	

Fig. 4. EPMA-WDS analyses of the cross-section of an LBM sample in the (XY) plane oxidised at 850 °C for 3000 h in static lab air.

alloy. It can also be noticed that, at P_{O_2} superior to 10^{-25} atm, the niobium oxide NbO_2 is stable, along with the chromia and a small quantity of TiO_2 . This is consistent with the Nb oxide observed in the chromia scale even though the $TiNbO_4$ phase is not predicted by

Thermocalc™ ($TiNbO_4$ is not in the TCNi9 database). $TiNbO_4$, which was identified by diffraction as a rutile-type structure, results from a mixture of NbO_2 and TiO_2 , both having a rutile-type structure. At higher P_{O_2} , Cr_2O_3 is still the most stable oxide, along with TiO_2 and

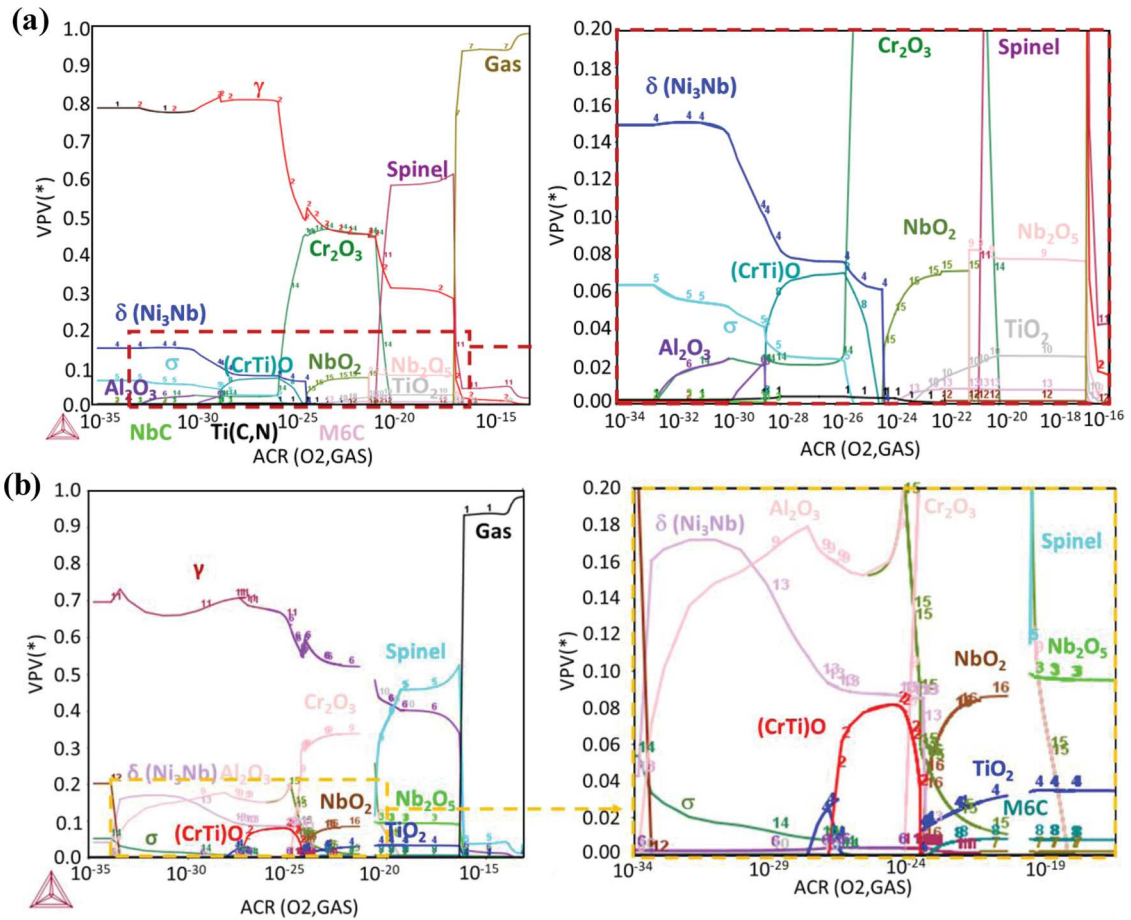


Fig. 5. Volume fraction of stable phases present in alloy 718 at 850 °C as a function of oxygen partial pressure, Thermocalc calculation (TCNi9) a) for the nominal composition of alloy 718, b) for the composition of the Cr-depleted area below the oxide scale experimentally measured.

Nb_2O_5 . The metallic γ phase (pure Ni at this stage) is still present up to 10^{-13} atm. Therefore, all these results can be considered as pertinent for the alloy below and close to the metal/oxide interface. For P_{O_2} superior to 10^{-13} atm, all the metal is oxidised. If a sample of alloy 718 is fully oxidised in a high oxygen pressure atmosphere, it should result in a spinel oxide $((\text{Ni,Fe})(\text{Cr,Fe})_2\text{O}_4)$ with a small quantity of halite NiO , Nb_2O_5 and TiO_2 .

When oxidising alloy 718, an enrichment in Nb was observed in the metal underneath the oxide scale. As stated in [32], this is due to thermokinetic reasons. The region underneath the oxide scale is also depleted in Cr due to the formation of a protective chromia scale. Therefore, the same thermodynamic calculation was done, but this time not with the composition of the LBM-718 alloy but with the composition of the alloy below the oxide scale formed after 3000 h at 850 °C. This composition, given in the lower part of Table 1, was measured by quantitative SEM-EDX on the LBM sample and by averaging the composition in three rectangle areas of $125 \times 6 \mu\text{m}^2$ directly under the external scale. Underneath the oxide scale, the concentration of Cr dropped since Cr was used to form the external- Cr_2O_3 scale. Conversely, Al and Ti concentrations increased because they were drained from deeper in the alloy to form Al_2O_3 or TiO_2 at the grain boundaries under the oxide scale.

Fig. 5(b) shows the result of the second thermodynamic evaluation, using the composition of alloy 718 depleted in Cr but enriched in Al and Ti. It can be seen that the sequence of oxide phases remains the same but their quantities have changed. Indeed, the smallest P_{O_2} values ($P_{\text{O}_2} < 10^{-25}$ atm) lead to higher quantities of Al_2O_3 and δ phase, as compared to the results of the first calculation. For P_{O_2} higher than 10^{-25} atm, the quantity of Cr_2O_3 and spinel decreases slightly, whereas the quantities of rutile oxides, TiO_2 and NbO_2 , increase slightly.

To summarize, the thermodynamic evaluations were done using the composition of alloy 718, either using the bulk composition or the composition of the Cr-depleted area under the oxide scale. Even if the calculations do not represent directly the gradient of microstructure in an oxidized sample, because they do not take into account the diffusion of the alloying elements such as the upward diffusion of Cr, they reveal that the different oxides were found from the bulk to the surface in the order corresponding to the increasing oxygen activity. Al_2O_3 forms deeper in the alloy, TiO forms at slightly higher P_{O_2} where chromia is not stable. At P_{O_2} higher than 10^{-25} atm, Cr_2O_3 oxide is stable and it is shown that NbO_2 and TiO_2 (and then probably NbTiO_4) are thermodynamically stable in contact with Cr_2O_3 . At high P_{O_2} (above 10^{-13} atm), all the metal is oxidised, the spinel phase $((\text{Ni,Fe})(\text{Cr,Fe})_2\text{O}_4)$ is formed in equilibrium with Cr_2O_3 and TiO_2 . This means that the spinel phase will form in the outer part of the chromia scale if enough Fe and Ni cations can diffuse outward through the chromia layer. Similarly, TiO_2 will form on the chromia scale if the outward diffusion of Ti is sufficient. Variations in alloy composition due to Cr depletion, or small composition changes due to different powder compositions or loss of some elements during AM, are unlikely to change the microstructure of the oxide scale.

3.2. External oxide scale and intergranular oxidation quantification and kinetics

3.2.1. Quantification of the oxide scale thickness and GBO by SEM image analysis

SEM image analysis was conducted to quantify external oxide scale thickness, GB oxide penetration depth and intergranular oxide thickness, as explained in §2. To do so, images similar to Fig. 3 were used. Results are presented in Fig. 6. After 3000 h at 850 °C, as shown in Fig. 6(a), the oxide scale on the LBM sample was found to be a little thicker ($8 \mu\text{m}$) than those found on EBM and wrought samples ($6 - 7 \mu\text{m}$). This could explain the slightly larger mass gain found in the LBM sample in Fig. 1. Moreover, as seen in Fig. 6(b), the penetration depth of GBO increased with oxidation time. The morphology of GBO

appeared more heterogeneous in the AM samples than in the wrought alloy. For instance, AM samples showed the deepest penetration of oxides at grain boundaries despite the fact that all samples presented a similar GBO depth average. In Fig. 6(c), it can be noticed that the two AM samples present the thickest oxide at the grain boundaries. This quantification confirms what can be seen in Fig. 3.

However, as presented Fig. 6(d), the three samples showed similar average of “GBO-to-scale equivalent thickness”. This parameter was defined from the cross-section as the measured area of oxides formed at GB over the length of the sample surface. This corresponds to the quantity (in terms of area) of oxide in the grain boundaries for a given sample surface area. With this parameter, it is possible to compare the mass gain resulting from the formation of the external scale with the mass gain resulting from internal and intergranular oxidation. For the samples oxidised for 3000 h, the quantification of the intergranular oxidation was conducted in the two main plans: (XY) perpendicular to the building direction and (XZ) parallel to the building direction. It was observed that the depths of intergranular oxidation were similar whichever the building plan, Fig. 6(b). However, in the (XZ) plan, which is parallel to the building direction, one can see the elongated grains that grew along the building direction. From that, the intergranular oxidation followed the GB of these grains and the GBO appeared on a longer distance as compared to what was found in the (XY) plan, but GBO did not go deeper in the alloy. This is an indication that GB oxidation kinetics is not controlled by the depth of the GBO penetration, i.e. not controlled by diffusion along the oxides formed at the alloys’ grain boundaries.

The three materials exhibited almost the same quantity of oxide at the alloy GB, but the oxide was thicker and the maximum depth was greater in AM samples than in the wrought sample. The occurrence of deeper GBO in samples fabricated by additive manufacturing could be detrimental to mechanical properties such as tension and fatigue.

3.2.2. Formation of voids

After 3000 h of oxidation at 850 °C, AM samples displayed voids ($\text{Ø}2\text{--}\text{Ø}15 \mu\text{m}$) in the Cr and δ -phase depletion zone in the grains or at the grain boundaries, especially in the EBM samples, as seen Fig. 7. Some of these voids might have been present in the as-built samples with a small size ($< \text{Ø}5 \mu\text{m}$) due to trapped gas bubbles and could have grown during the oxidation test. The growth of voids may result from vacancies injection due to oxidation and/or from a Kirkendall effect due to the Cr-depleted zone under the oxide scale in Ni-Cr alloys [22]. Both phenomena can act simultaneously, vacancies can be injected in the alloy due to Cr consumption to form the oxide scale, and the resulting vacancies in the metal can be “pushed” towards the bulk of the sample because the Cr flux towards the oxide scale is faster than the Ni flux in the opposite direction. The vacancies coalesce to form voids where their oversaturation is maximum and where pre-existing defects favour void nucleation. Nevertheless, these voids were not present in the wrought alloy. This can be explained by the fact that during the hot forming process, the grains were distorted thereby inducing recrystallization and crystal defects such as dislocations [36]. Pieraggi *et al.* [37] showed that the annihilation of vacancies can be done by a climbing and gliding mechanism of interfacial dislocations next to the metal/oxide interface or by removing dislocation loops without formation of voids. Whereas, in materials containing a low density of dislocations and pre-existing small voids, the annihilation of vacancies is easier by growing pre-existing voids. Since both intergranular oxidation and voids formation can act as crack-initiation sites and consequently affect the mechanical behaviour of materials, it is therefore important to quantify and model this intergranular oxidation in order to better predict mechanical behaviour.

3.2.3. GBO kinetics

Fig. 8 shows the kinetics of the intergranular oxidation in terms of average GBO penetration depth as a function of time. It can be seen that

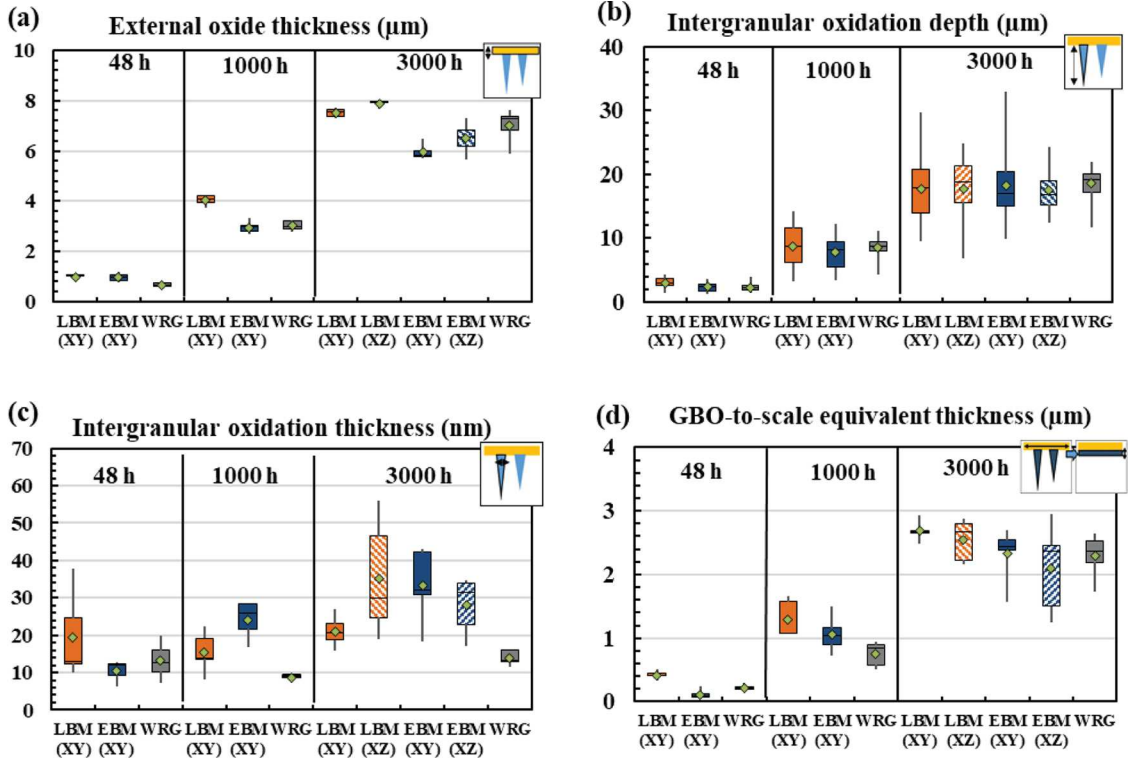


Fig. 6. Quantification of intergranular oxidation by micrograph analyses of the cross-section of oxidised LBM, EBM and wrought samples in the (XY) plane oxidised 48 h, 1000 h and 3000 h in air.

GBO kinetics can be interpreted either as following linear kinetics after a transient regime of fast oxidation, or as parabolic kinetics with a lower fitting accuracy but with no transient regime. Linear kinetics would mean that GBO growth is controlled by the reaction rate at the tip of the penetration. Whereas parabolic kinetics would imply a process controlled by diffusion, which could either be the diffusion of O towards the tip of the penetration, or the diffusion of Al and Ti from the bulk towards the extremity of oxides formed at the GB, or both. At this stage, there is not enough data to clarify this point. Nevertheless, it is possible to suppose that the process is controlled by diffusion, as it is often the case in internal oxidation [38].

To verify this mechanism, oxidation kinetics must be consistent with independent evaluations, such as the determination of diffusion coefficients. With the assumption of parabolic kinetics, parabolic rate constants k_{PGBO} ($\mu\text{m}^2\text{h}^{-1}$) were determined from Eq. (2), they correspond to the slope of the linear fit of the parabolic plots in Fig. 8(b).

$$d_{GBO} = \sqrt{k_{PGBO} \cdot t} \quad (2)$$

The values of k_{PGBO} are presented in Table 2.

GBO is known to induce intergranular embrittlement leading to intergranular fatigue crack propagation. Therefore its maximum depth value is a key parameter to consider and the $k_{PGBOmax}$ corresponding to the maximum GBO depth were calculated and presented in Table 2. Results show that in terms of average GB oxide penetration, the three alloys have similar GBO kinetics, as indicated by the k_p (mass variation) and k_p' (oxide thickness). After 3000 h at 850 °C, all alloys presented a k_{PGBO} of about $1.0 \times 10^{-1} \mu\text{m}^2\text{h}^{-1}$ for an average GBO depth close to 18 μm . As for maximum GBO depth however, the AM samples' (34- μm deep) was twice as deep after 3000 h of oxidation as the wrought sample's (19- μm deep).

The values of k_{PGBO} were compared to those estimated based on literature results [1–3,7–9,16,19,20,29,30,32,39–46] and plotted in an Arrhenius plot shown in Fig. 9. Values of k_{PGBO} from the literature were

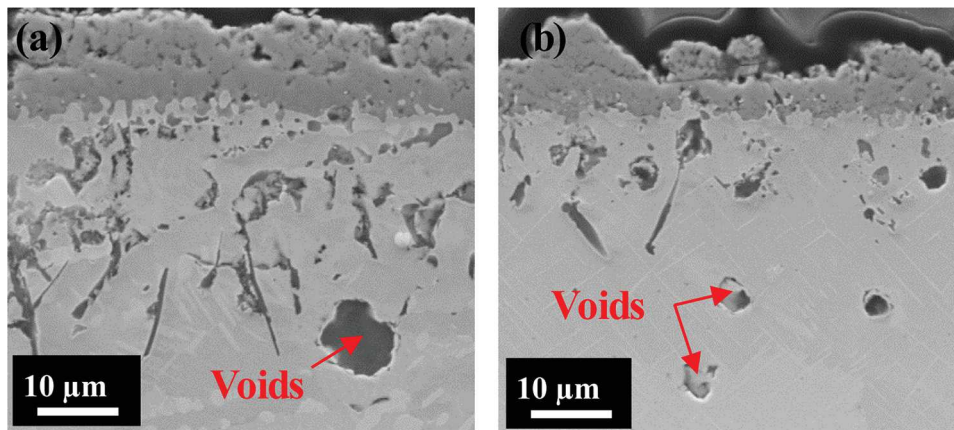


Fig. 7. SEM-SE micrographs of the cross-section of oxidised (a) LBM and (b) EBM samples, both ground with P600 SiC paper, for 3000 h in static lab air.

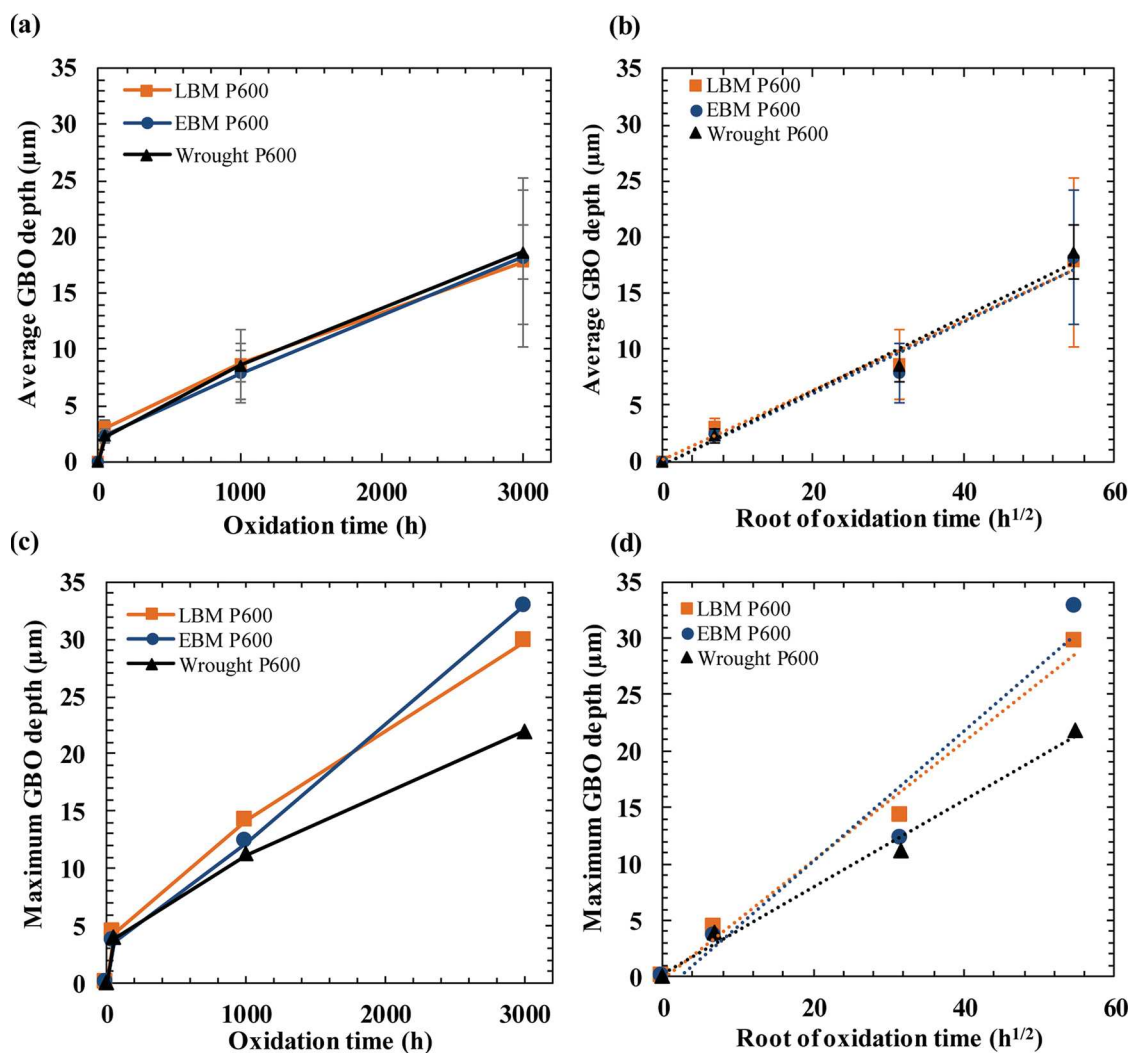


Fig. 8. Isothermal intergranular oxidation kinetics of the three alloys 718 (LBM, EBM, wrought) at 850 °C for 48 h, 1000 h and 3000 h (the 48 h experiments were conducted in TGA under synthetic air flow, the others in static lab air). Graphs a) and b) relate to average GBO depth. Graphs c) and d) relate to the maximum value of GBO depth.

calculated by measuring ourselves GBO depths from micrographs presented in the published papers. Compared to alloy 718 samples produced by LBM by Jia and Gu, and studied at the same temperature of 850 °C under still laboratory air [2], the as-built LBM and as-built EBM samples studied here presented a much better resistance to intergranular oxidation. This difference can be explained by important differences in material density. Moreover, regarding the k_{PGBO} determined from the average of oxide penetration depth, the intergranular oxidation resistance of our samples was similar to that of alloy 718 produced by EBM and studied by Juillet *et al.* [44], and to that of alloy 718 produced by LBM and studied by Calandri *et al.* [45]. In addition, further works on alloy 718 at higher temperatures [1,40,46] led to the determination of the activation energy of GBO for alloy 718 between 800 °C and 1050 °C. This value was estimated at 268 kJ mol⁻¹.

At lower temperatures – such as those used in the nuclear field – k_{PGBO} values are orders of magnitude higher than what could be expected from the extrapolation based on high temperatures. Therefore, the mechanisms controlling GBO kinetics is certainly different at high (> 800 °C) and low (< 400 °C) temperatures.

3.3. Influence of microstructure on GBO

Quantitative WDS and EBSD analyses were conducted to evaluate the impact of microstructure on intergranular oxidation. The first

objective was to understand the difference in GBO between the AM samples and the wrought sample (GBO thickness and maximum depth). Four topics were discussed, namely crystallographic texture, grain size, grain misorientations and nature of grain boundaries.

3.3.1. Effect of alloy texture

Fig. 10 presents the EBSD analysis of the subsurface beneath the oxide scale. Results show that AM samples present a strong crystallographic texture with the $\langle 100 \rangle$ direction along the growth direction, which was already found in other studies [47,48]. This is due to the temperature gradient during the layer-by-layer melting process. A difference in texture can be observed between LBM and EBM samples. They both have a preferential orientation $\langle 100 \rangle$ in the growth direction, but the LBM sample also has a preferential orientation $\langle 100 \rangle$ perpendicular to its oxidised surface, this is not the case for the EBM sample.

On the other hand, the heat-treated wrought sample shows only a slight preferential $\langle 111 \rangle$ orientation, perpendicular to the cross section. The influence of the crystallographic texture of a Haynes 230 superalloy on oxidation was investigated by Xu *et al.* [49]. They showed that surfaces parallel to $\{111\}$ planes have a better oxidation resistance than those parallel to $\{110\}$ or $\{100\}$ planes. Nevertheless, this result was only noticed during the early stage of the oxidation, after 5 min at 900 °C, and did not affect GBO. In addition, the comparison of the

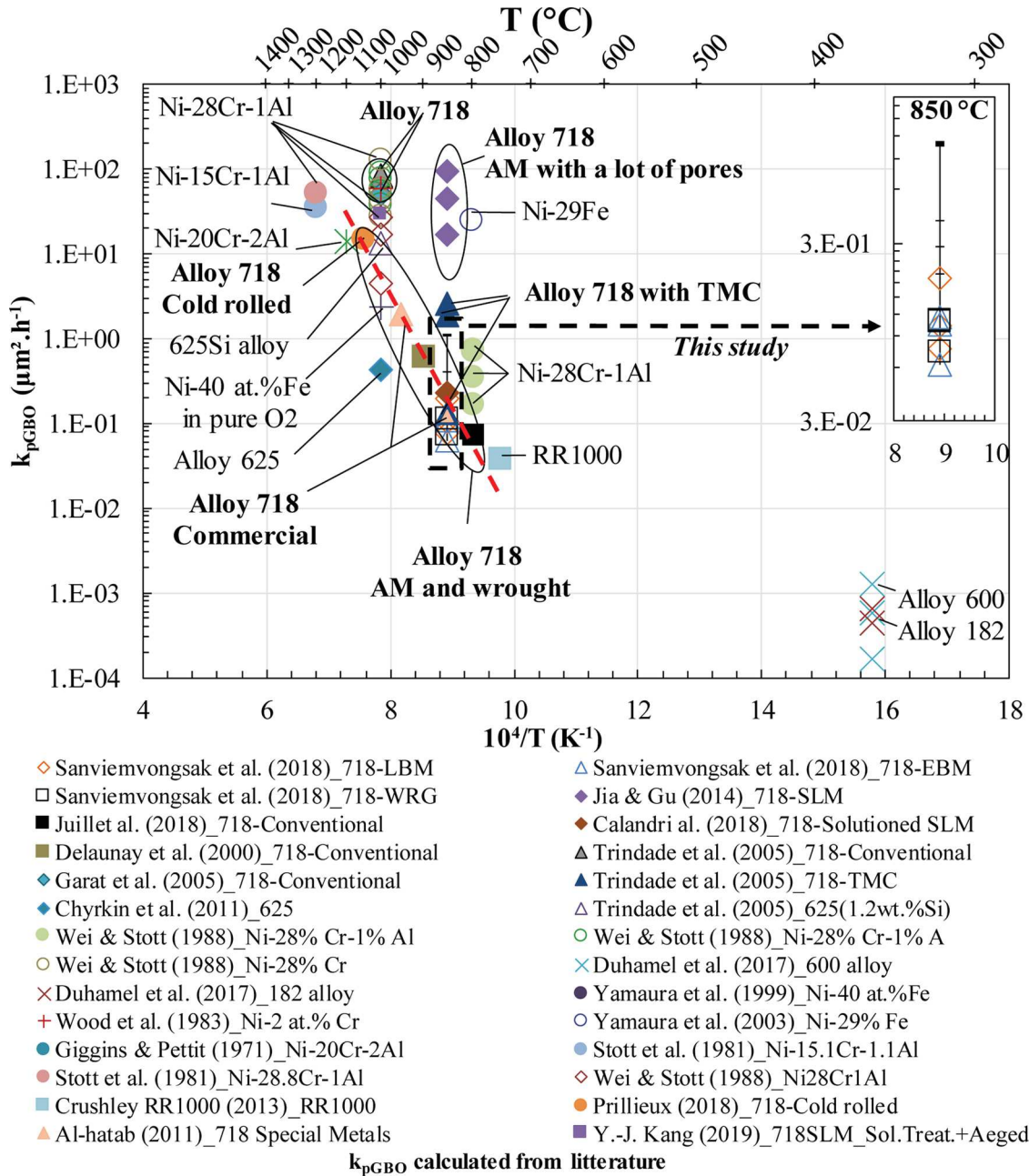


Fig. 9. Arrhenius diagram of the parabolic constant k_{pGBO} found in this study, compared to values calculated from images published in the literature [1–3,7–9,16,19,20,29,30,32,39–46] (TMC for Thermomechanical compression).

intergranular oxidation in the two planes (XY) and (XZ), in Figs. 3 and 6, shows similar intergranular oxidation depths and similar intergranular oxidation equivalent thicknesses. For these reasons, the general crystallographic texture should not have a significant impact on GBO.

3.3.2. Effect of grain size

In Fig. 10(d)–(f), it can be noticed that LBM and wrought samples presented similar average grain size, close to 10 μm . The EBM sample presented the largest grains, 17 μm in average in the subsurface zone beneath the oxide scale, but the LBM sample also presented some grains with diameters larger than 30 μm , as seen in Fig. 10(d). From Figs. 3 and 6 it was shown that both LBM and EBM samples presented thicker intergranular oxidation compared to the wrought sample. The EBM sample presented the deepest and thickest intergranular oxides as well as the largest grain sizes.

The influence of grain size on the thickness of the oxides formed at the grain boundaries was then investigated. Analyses were conducted on 100 grain boundaries with oxide penetration in each AM sample, and on 50 grain boundaries with oxide penetration found in the wrought sample. In Fig. 11(a), results show that there is a very light correlation between grain size and GB oxide thickness. The bigger the grains on each side of the GBO, the thicker the oxide at the grain boundaries. This result can be easily explained by the fact that the quantity of elements needed for the growth of the intergranular oxide, i.e. Al or Ti, is higher in the biggest grains and can induce a larger lateral growth of the intergranular oxide. In addition, as seen in Table 1 the quantity of Ti and Al in the AM samples (2.2 at. %) is slightly higher than in the wrought alloy (1.9 at. %). This could also explain the thicker GBO of AM samples. The quantitative WDS analysis in Fig. 12 shows that all the Al and Ti contained in the grain next to the GBO was consumed to form the oxide at the grain boundaries. Aluminum thus

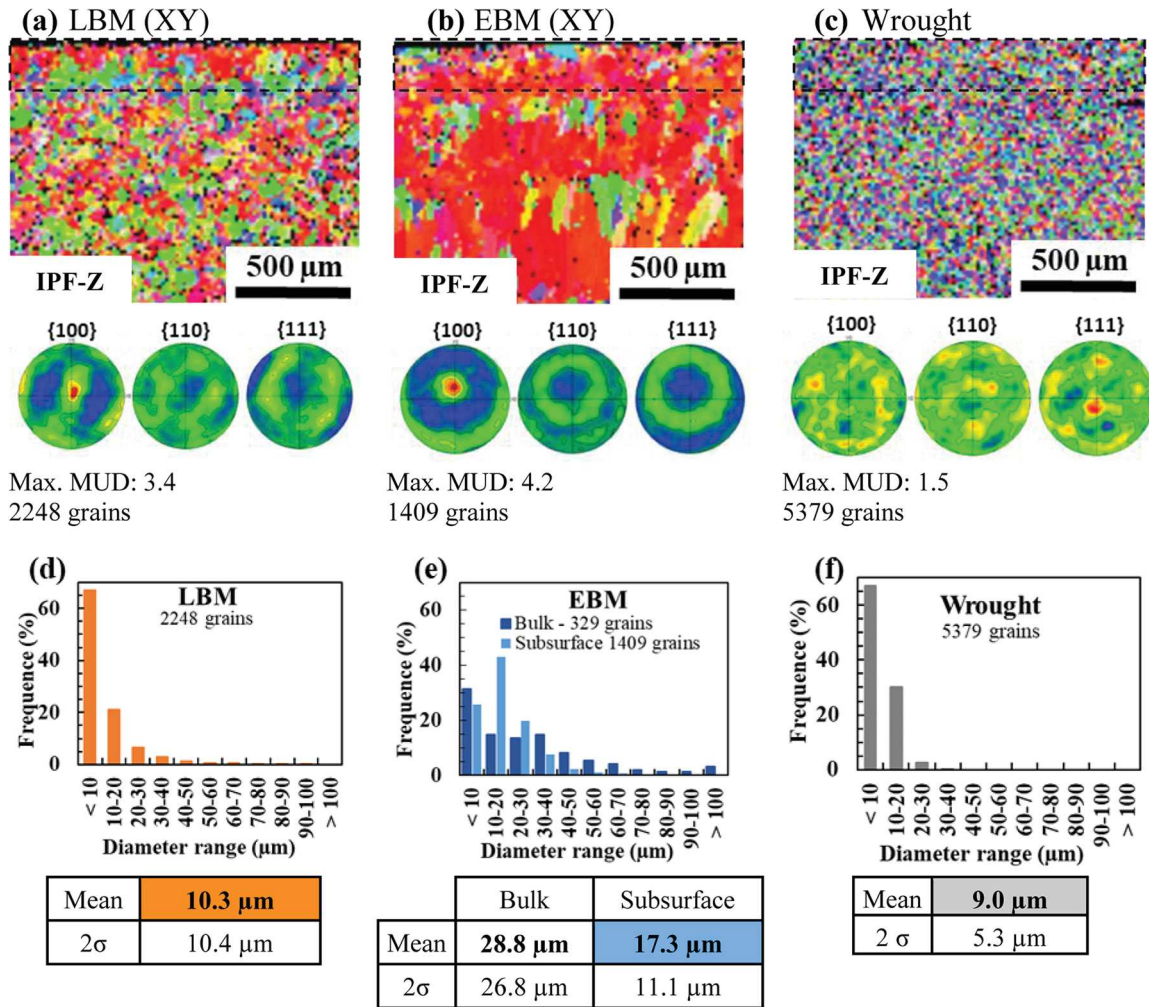


Fig. 10. EBSD-SEM micrographs and pole-figures of a cross-section of the subsurface zone of samples oxidised 3000 h in static lab air of (a) LBM, (b) EBM and (c) wrought samples in the (XY) plane. Grain diameter distribution of the analysed subsurface of (d) LBM, (e) EBM and (f) wrought samples.

diffuses laterally in the grain to contribute to the lateral growth of the GBO. In addition, the depletion of Al in the grain can reach 70-µm deep, which is deeper than the average depth found for intergranular oxidation. Deeper in the alloy, Al and Ti diffuse towards the closest GB and then diffuse quickly outward in the GB towards the tip of the penetration, where they react with O diffusing inward from the external oxide scale, along the intergranular oxides.

3.3.3. Effect of GB misorientation and special grain boundaries

The impact of grain misorientation on the quantity of oxide in the grain boundary was evaluated. Here again, as for the grain size, the correlation is very low, as seen in Fig. 11(b). There is a very slight increase in the amount of oxide in these grain boundaries with the misorientation between grains in the AM samples. Although this result seems to be consistent in AM samples, it is not true for wrought samples and cannot be used to justify the difference between AM and wrought

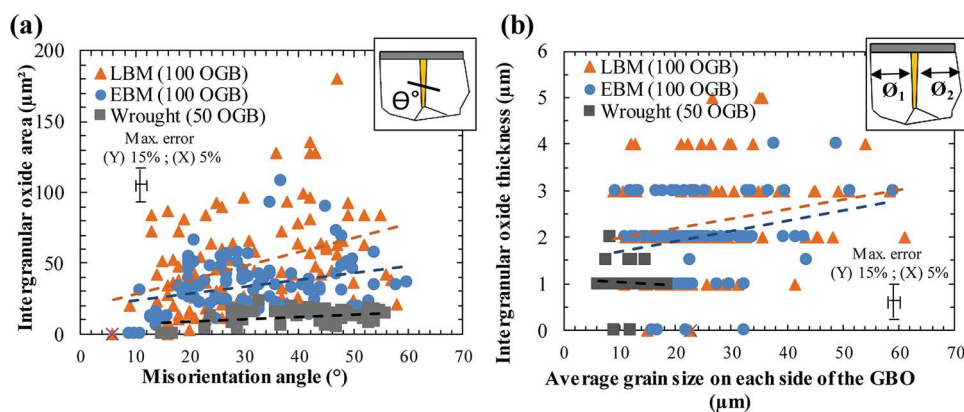


Fig. 11. Correlation graphs used to identify (a) the impact of the misorientation angle between the two grains on each side of the GBO on the intergranular oxide area, and (b) the impact of GBO grain size on intergranular oxide thickness. Analyses conducted on samples oxidised in air at 850 °C for 3000 h.

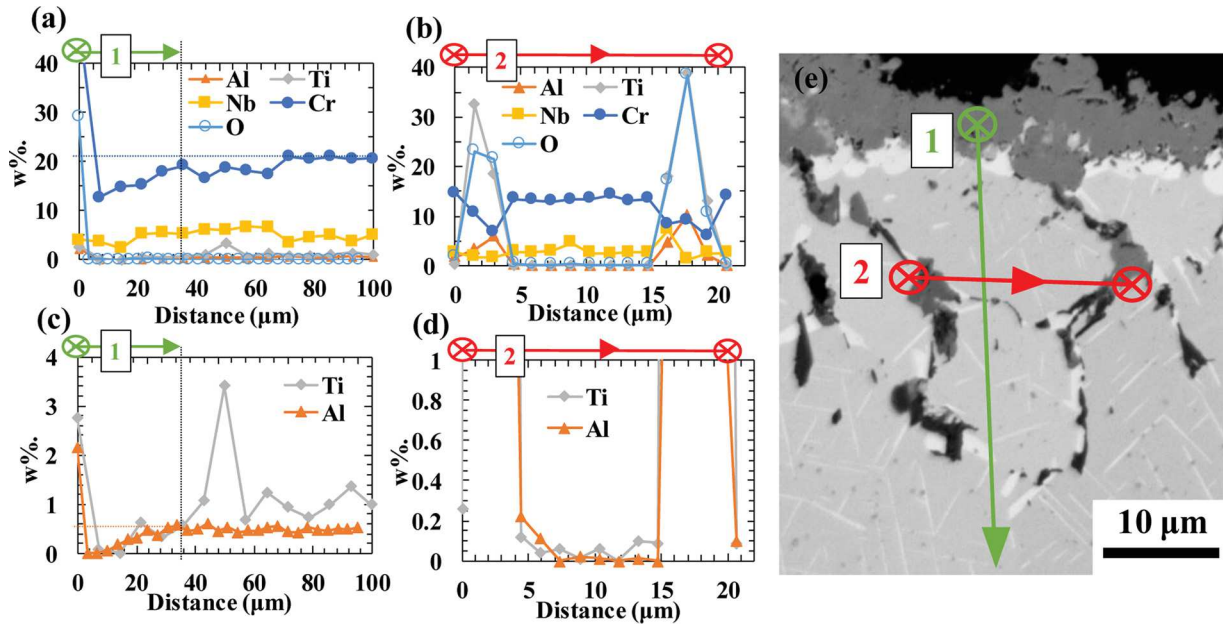


Fig. 12. EPMA-WDS profile analysis of a cross-section of the EBM sample in the (XY) plane oxidised 3000 h in static lab air (profiles for LBM and wrought samples are similar).

samples.

Another crystallographic factor could explain the wrought alloy's better resistance to intergranular oxidation. It can be seen in Fig. 13 that the wrought sample presented a high proportion of special grain boundaries. Special grain boundaries are defined as boundaries with a high number of coincident sites in the coincident sites lattice (CSL) characterized by a low Σ factor [50]. In the wrought sample, around 30 % of the grain boundaries detected are special boundaries, against 3 % and 9 % found in LBM and EBM samples respectively. Among the special boundaries detected in the wrought alloy, 25 % were $\Sigma 3$ -twin boundaries. Krupp *et al.* [9] showed that special grain boundaries found on a wrought alloy 718 containing a high fraction of special grain boundaries such as $\Sigma 3$ -twin boundaries, had a better oxidation resistance as compared to random grain boundaries. This result was also found later by Kobayashi *et al.* on the corrosion behaviour of SUS316 L austenitic steel [51]. It was proposed in the literature that these results could be explained by the fact that O diffusivity is much slower in special grain boundaries [52].

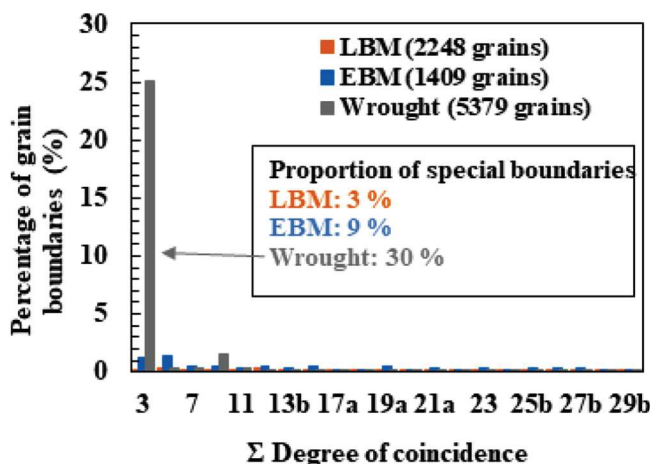


Fig. 13. Proportion of special grain boundaries in the subsurface zone determined by EBSD analysis of LBM, EBM and wrought samples oxidised 3000 h in static lab air.

3.3.4. Effect of alloy GB chemistry

The chemical composition of grain boundaries affects alloy properties, it is therefore important to understand how it can result in alloy improvement. Sun *et al.* [53] found that phosphorus, introduced in the range of 0.0008–0.013 wt. %, enhanced intergranular oxidation resistance. P segregates in the alloy grain boundaries and could limit not only O diffusion [53] but also Al and Ti diffusion. As a consequence, GBO appeared thinner and less deep when increasing P concentration. Other GB segregants, such as S, B, C or N, could also have an effect. This could be an explanation as to the difference in intergranular oxidation between AM samples and the wrought alloy, but further high-resolution, atomic-scale characterisations would be necessary to measure the composition at GBs, and presently nothing particular was noticed in the bulk composition of the 3 alloys regarding these impurities.

3.4. Discussion on the intergranular oxidation mechanism

3.4.1. Proposal of a general mechanism of GBO for alloy 718

The schematic diagram in Fig. 14 shows the intergranular oxidation mechanism discussed throughout this paper and supported by qualitative observations. After 48-h oxidation tests at 850 °C, alloy 718, whether additively manufactured or wrought, presented an external scale of chromia and intergranular oxides TiO_2 and Al_2O_3 , as shown in Fig. 3. Chromium diffused from the bulk towards the alloy surface, through the grains and the GBs of the alloy, and reacted with O to form an external chromia scale. The grain boundaries are known to act as diffusion short-circuits, this is why the external scale looks like a blister directly above the alloy grain boundaries, indicating that Cr diffusion limits, at least partially, the growth kinetics of the oxide scale.

In the material, at this temperature and with this O partial pressure, Al and Ti contents are sufficient to trigger the reaction with O and were oxidised preferentially, as seen in Fig. 5. On the other hand, the concentrations and diffusion coefficients of Al and Ti are not high enough, in other words the fluxes of these elements towards the surface are not sufficient to form a continuous external scale. Therefore, Al and Ti oxides form internally.

The diffusion of O is not fast enough in the bulk of the grains to form internal oxides disconnected from the external oxide deep in the alloy. But the diffusion of O along GBO/metal interfaces and the diffusion of Al and Ti in metal GBs are fast enough for the intergranular oxide to

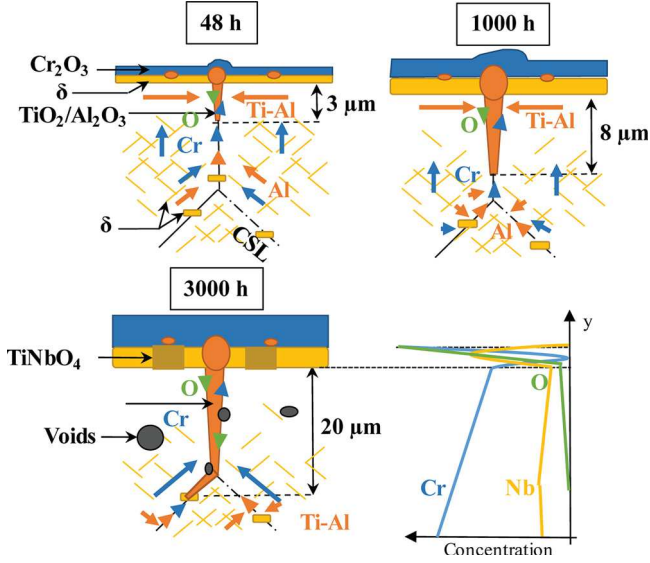


Fig. 14. Schematic diagram explaining the intergranular oxidation mechanism of AM alloy 718 at 850 °C for different oxidation durations (48 h, 1000 h, 3000 h).

grow. Because diffusion in GB is involved, no GBO was observed in the special grain boundaries (CSL), as found in the following references [8,9,43,52].

The Nb present in the bulk and at GBs as γ' and δ precipitates, diffuses outward, similarly to Cr. This is due to the gradient of chemical potential caused by Cr depletion, which acts as a driving force for Nb diffusion [32]. Then, the increasing Nb concentration below the oxide scale induced a re-precipitation of the δ phase below the oxide scale. After 1000 h of oxidation, the oxide scale and the Nb-rich layer grew, the intergranular oxidation became thicker and deeper, as well as Cr and Nb depletions. After 3000 h of oxidation and from EPMA-WDS analyses (Figs. 4 and 12), and consistently with thermodynamic calculations in Fig. 5, it can be concluded that the Nb began to oxidise. Rutile-type TiNbO_4 was identified by EBSD.

Regarding the intergranular oxidation mechanism, the EPMA-WDS profile (1) in Fig. 12 shows that Al and Ti concentrations dropped to zero inside the grain. This means that these elements diffused laterally toward the GB to contribute to the lateral growth of intergranular TiO_2 and Al_2O_3 .

In Fig. 12 profile (2), the Cr-depleted zone reached a depth of $65 \pm 5 \mu\text{m}$ and the Al-depleted zone reached $38 \pm 5 \mu\text{m}$, which is much deeper than the average depth of intergranular oxidation ($18 \pm 10 \mu\text{m}$ deep). This result shows that, deep in the alloy bulk, Al atoms diffuse toward the closest GB and then diffuse upward in the GB to react with O at the tip of the deepest grain boundary oxides. As a consequence, the diffusion of Ti, Al and Nb, induced the dissolution of hardening precipitates such as γ' , γ'' and δ phases. The Al-depleted zone reached a depth of $40 \mu\text{m}$ which could have an impact on the mechanical properties of the alloy.

3.4.2. Confrontation of the GBO model with quantitative data

This overall mechanism can be confronted with the available diffusion data. Table 3 presents the activation energies found in the literature and the estimated value of the diffusion coefficients and diffusion depths of several elements in the volume or in the GBs. This table was used to identify the mechanism that could control intergranular oxidation kinetics.

In Fig. 9, the activation energy of the intergranular oxidation of alloy 718 was evaluated at about 268 kJ mol^{-1} . This value is close to the activation energy of O diffusion through nickel alloy GBs [11,12], but also close to the activation energy of the diffusion of Ti in FCC-

NiTiAl (polycrystal) [54] or of Al in FCC-Ni (polycrystal) [55]. Moreover, by comparing calculated diffusion depths (given by $2\sqrt{Dt}$), it is clear that the diffusion of O in a Ni-base fcc polycrystal lattice and the diffusion of Ti or Al in GBs, are much faster than the diffusion of Ti or Al in the volume.

In order for the intergranular oxide to grow, it is necessary that both O and Al (or Ti) reach the tip of the penetration at the grain boundaries. When O reaches the extremity of the oxide formed at the GB, it reacts with the Al to form a continuous intergranular oxide. If Al was not present in sufficient quantity at the tip of the oxide formed at the GB, then this oxide would not be continuous. This result means that the Al flux towards the extremity of the GBO penetration is at least as large as the inward O flux. The Al flux towards the tip of the GBO penetration depends on its diffusion in the GB free of oxide, below the intergranular oxide, but also on its diffusion in the bulk of the alloy to reach the grain boundaries.

By applying Wagner's theory of internal oxidation [38], the oxidation kinetics of a binary alloy (AB) is controlled by both inward O diffusion and outward diffusion of B, in our case Al. The internal oxidation kinetics can be described by Eq. (3) below:

$$k_p^{(O)} = \frac{\pi}{D_B} \left(\frac{D_O N_O^{(s)}}{2\nu N_B^{(O)}} \right)^2 \quad (3)$$

$$k_p^{(O)} = z^2 \times \frac{1}{t} \quad (4)$$

With $k_p^{(O)}$ the internal oxidation parabolic rate constant ($\text{cm}^2 \text{s}^{-1}$), D_B and D_O ($\text{cm}^2 \text{s}^{-1}$), respectively the diffusion coefficient of Al and O in the alloy that were found in the literature and reported in Table 3. In our case, N_B corresponds to the concentration of Al in alloy 718 ($N_{Al} = 1 \text{ at. \%}$). N_O corresponds to the solubility limit of O in the alloy without B. z (cm) corresponds to the depth of the zone affected by internal oxidation. The stoichiometric coefficient ν is determined with the following reaction:



The solubility limit of O within the alloy was determined using the ThermoCalc software with the TCNi9 Ni-database. Thermodynamic calculations were conducted with the chemical composition of alloy 718 measured by EDX below the external oxide scale (52.7Ni, 19.8Fe, 9.5Cr, 5.7Nb, 3.7Mo, 0.1Co, 0.05 Mn, in wt. %) without Al and Ti which were oxidised. The O partial pressure found at the chromia oxide scale/metal interface at 850 °C was $P_{O_2} = 7.4 \times 10^{-26} \text{ atm}$ and the corresponding O concentration in the alloy in equilibrium with the oxide scale was calculated: $N_O = 6.2 \times 10^{-5} \text{ at.ppm}$.

The penetration depth z of the internal oxidation was estimated from Wagner's formula Eqs. (3) and (4). Several combinations of O and Al diffusion coefficients in nickel or nickel alloys (Table 3) were tested. Results in Table 4 show that if we consider that O diffuses in the volume ($D_{O,vol}$) and that Al (D_{Al}) diffuses either in the volume or in the grain, the value of the internal oxidation depth (z) for a 3000-h oxidation at 850 °C is much too small compared to our observations. On the contrary, if we consider that O diffuses at the intergranular oxide/metal interface ($D_{O,interf}$) and that Al diffuses either in the metal volume or in the alloy grain boundaries free of oxide, it is possible to find a realistic value for $D_{O,interf}$. This results in an intergranular oxidation penetration depth of 23 μm , which is close to the experimental results. To reach a depth of 23 μm , if we consider that Al diffusion at the alloy GBs ($D_{Al,GB}$) controls the kinetics, the O diffusion value must be set to $D_{O,interf} = 8 \times 10^7 D_{O,vol}$. If we now consider that kinetics are controlled by Al diffusion in the volume of the alloy grains ($D_{Al,vol}$), the value must be set to $D_{O,interf} = 2.2 \times 10^5 D_{O,vol}$. This latter value is consistent with the diffusion coefficient of O at the intergranular oxide/metal interface found in the literature. Indeed, Stott *et al.* [14] estimated that O diffusion at Al_2O_3 internal oxide/nickel matrix incoherent interfaces was 1.2×10^4 times faster than O diffusion in the bulk at 1100 °C, and

Table 3

Diffusion data on Ni-base fcc alloys from the literature: pre-exponential factors, activation energies. Diffusion coefficients and diffusion depths were determined at 850 °C after 3000 h.

Elements	Temperature (°C)	Pre-exponential factor D_0 (cm ² /s)	Activation energy Q_a (kJ/mol)	Diffusion coef. at 850 °C D (cm ² /s)	Diffusion depth 850 °C-3000 h $2\sqrt{Dt}$ (μm)	Ref.
O in Ni (Polycrystal)	850–1400	4.90×10^{-2}	164	1.14×10^{-9}	2222	[10]
O in Ni (Polycrystal)	1000–1150	$3.63 \times 10^{+4}$	277	4.67×10^{-9}	4490	[56]
Cr in Ni-20.4Cr (Polycrystal)	950–1360	2.10×10^{-1}	249	5.48×10^{-13}	49	[57]
Nb in Ni (Polycrystal)	927–1227	1.04×10^{-2}	203	3.88×10^{-12}	129	[58]
Ti in Ni-76 % TiAl (Polycrystal)	900–1200	2.40	267	9.01×10^{-13}	62.4	[54]
Al in Ni (Polycrystal)	996–646	4.40×10^{-1}	245	1.74×10^{-12}	87	[55]
Al in Ni (GB)	200–287	7.10×10^{-2}	120	1.85×10^{-7}	28,256	[59]
Ni in Ni (Polycrystal)	927–1227	1.27	281	1.07×10^{-13}	22	[58]
Ni in Ni (GB)	700–1250	5.40×10^{-2}	123	1.02×10^{-7}	20,984	[60]

Table 4

Calculated intergranular oxidation kinetics for different diffusion paths of O and Al. $k_p^{(O)}$ and z were determined for a 3000-h oxidation at 850 °C using Wagner's theory on internal oxidation and Thermocalc (TCNi9) values $P_{O_2}^{850,718} = 7.4 \times 10^{-26} \text{ atm}$ and $N_O^{850,TC,718} = 6.2 \times 10^{-5} \text{ at. ppm}$.

Diffusion paths for O and Al:	Al (Poly.) and O (Poly.)	Al (GB) and O (Poly.)	Al (Poly.) and O (GB)	Al (GB) and O (GB)
$k_p^{(O)}$ (cm ² s ⁻¹)	1.0×10^{-23}	9.4×10^{-29}	4.9×10^{-13}	4.6×10^{-18}
z (μm)	1.0×10^{-4}	3.2×10^{-7}	23	7.0×10^{-02}

2×10^4 times faster at 1050 °C.

In conclusion, the intergranular oxidation kinetics could be controlled by both the supply of O at the tip of the oxide formed at the GB through the intergranular oxide/metal interfaces and the supply of Al. Al must diffuse through the volume of the alloy grains before diffusing in the alloy grain boundaries up to the tip of the oxides formed at the GB. Because these two diffusion paths act in series, the slowest step, i.e. the diffusion of Al in the volume, controls the kinetics of the supply of Al.

4. Conclusions

The isothermal oxidation at 850 °C, in air, of as-built LBM and EBM samples of alloy 718 was compared to the oxidation of a wrought heat-treated (AMS5662) alloy 718.

- Oxidation kinetics in terms of mass gain or in terms of GB oxide penetration kinetics are close for AM samples and wrought alloy
- The mass gain of LBM samples was found to be 20 % higher than that of EBM and wrought samples. This was mainly attributed to a slightly thicker chromia scale, and a slightly higher quantity of intergranular oxidation. After a 3000-h oxidation test, the parabolic rate constants ranged from 0.4×10^{-7} to $1.8 \times 10^{-7} \text{ mg}^2 \text{ cm}^{-4} \text{ s}^{-1}$ which agrees well with the literature.
- After a long oxidation exposure (3000 h), the Nb present beneath the oxide scale/metal interface, oxidised. This oxide was identified as TiNbO₄ (rutile-type oxide). Calphad calculations with TCNi9 Ni-database are in agreement with the fact that TiO₂ and NbO₂ can coexist in equilibrium with Cr₂O₃.
- The morphology of the oxides formed at the grain boundaries in AM samples was found different than in wrought samples. GB oxides of AM samples were found less homogenous, thicker and with deeper penetrations than those found in the wrought samples which were found thinner and more homogenous.
- Intergranular oxidation kinetics of AM samples were slightly higher. However, the quantity of intergranular oxidation was not significantly different. The comparison of intergranular oxidation kinetics with those found in the literature showed that additively

manufactured samples in their as-built form have a competitive intergranular oxidation resistance when compared to a wrought or cast alloy 718.

- AM samples, which presented larger grain sizes, also presented thicker oxides at grain boundaries. This observation was explained by the full depletion of Al in the grains. Nevertheless, the quantitative correlation between grain size and GBO thickness was weak.
- The impact of crystallographic texture and misorientation of the two grains from either side of the GB, on the quantity of intergranular oxidation was not significant.
- The main difference between AM and wrought samples lies in the nature of their grain boundaries. Indeed, in the wrought sample, 30 % of grain boundaries analysed were special grain boundaries, against 3% and 9% in LBM and EBM samples respectively. These boundaries are known to have a better resistance to intergranular oxidation, which was confirmed in the present work.
- A general mechanism for 718 alloy intergranular oxidation was proposed. The WDS analysis of Al depletion and the GBO kinetics analysis showed that intergranular oxidation growth follows Wagner's internal oxidation theory, in which case GBO kinetics is controlled by both the diffusion of O in the GB oxide/metal interface and the diffusion of Al in the metal volume. For special GBs, the slower diffusion of Al and Ti in GBs participate in the control of GBO kinetics.
- A finer scale analysis of the chemical composition of grain boundaries should be carried out in order to identify the elements affecting intergranular oxidation resistance and to determine whether AM modifies intergranular chemistry.

CRedit authorship contribution statement

Tom Sanviemvongsak: Methodology, Investigation, Writing - original draft, Visualization. **Daniel Monceau:** Supervision, Validation, Writing - review & editing. **Clara Desgranges:** Formal analysis, Writing - review & editing. **Bruno Macquaire:** Resources, Funding acquisition, Writing - review & editing.

Declaration of Competing Interest

The authors declare that they have no known competing financial interests or personal relationships that could have appeared to influence the work reported in this paper.

Acknowledgments

The authors would like to thank Arnaud Proietti and Sophie Gouy, both from the Raimond Castaing Microanalysis Centre. We would like to thank them for their analysis and constructive discussions respectively for the EBSD results and EPMA-WDS results. This research was

supported by Safran Group under the direction of Safran Additive Manufacturing (SAM) team.

References

- [1] K.A. Al-hatab, M.A. Al-bukhaiti, U. Krupp, M. Kantehm, Cyclic oxidation behavior of IN 718 superalloy in air at high temperatures, *Oxid. Met.* 75 (2011) 209–228.
- [2] Q. Jia, D. Gu, Selective laser melting additive manufactured Inconel 718 superalloy parts: high-temperature oxidation property and its mechanisms, *Opt. Laser Technol.* 62 (2014) 161–171.
- [3] T. Sanviemvongsak, D. Monceau, B. Macquaire, High temperature oxidation of IN 718 manufactured by laser beam melting and electron beam melting: effect of surface topography, *Corros. Sci.* 141 (2018) 127–145.
- [4] E. Andrieu, R. Molins, H. Ghonem, A. Pineau, Intergranular crack tip oxidation mechanism in a nickel-based superalloy, *Mater. Sci. Eng. A* 154 (1992) 21–28.
- [5] R. Molins, G. Hochstetter, J.-C. Chassaing, E. Andrieu, Oxidation effects on the fatigue crack growth behaviour of alloy 718 at high temperature, *Acta Mater.* 45 (1997) 663–674.
- [6] H.E. Evans, H.Y. Li, P. Bowen, A mechanism for stress-aided grain boundary oxidation ahead of cracks, *Scr. Mater.* 69 (2013) 179–182.
- [7] V. Garat, O. Brucelle, J.M. Cloue, V. Rebeyrolle, D. Monceau, B. Viguier, E. Andrieu, Comparing different methods to determine the intergranular oxidation damage on a nickel based superalloy, *High Temperature Corrosion and Protection of Materials* 6, Part 1 and 2, Proceedings (2004) 537–544.
- [8] E.-G. Wagenhuber, V.B. Trindade, U. Krupp, The Role of Oxygen-grain-Boundary Diffusion During Intercrystalline Oxidation and Intergranular Fatigue Crack Propagation in Alloy 718 Superalloys 718, 625 and Various Derivatives, (2005).
- [9] U. Krupp, P.E.G. Wagenhuber, Y.M. Virkar, H.J. Christ, Studying the role of the alloy-grain-boundary character during oxidation of Ni-base alloys by means of the electron back-scattered diffraction technique AU - Trindade, V.B., *Mater. High Temp.* 22 (2005) 207–212.
- [10] J.-W. Park, C.J. Altstetter, The diffusion and solubility of oxygen in solid nickel, *Metall. Trans. A* 18 (1987) 43–50.
- [11] W. Chang, Superalloys-Processing, Proc. 2nd Intl. Conf. on Superalloys, Sec. V, in, MCIC-72-10, 1972.
- [12] R.G. Iacocca, D.A. Woodford, The kinetics of intergranular oxygen penetration in nickel and its relevance to weldment cracking, *Metall. Trans. A* 19 (1988) 2305–2313.
- [13] L.A. Ronqueti, J. Favergeon, M. Risbet, M. Picard, Study of grain boundary oxidation of high alloyed carbon steels at coiling temperature, 53rd Rolling Seminar (2016) 283–292.
- [14] F.H. Stott, G.C. Wood, Internal oxidation, *Mater. Sci. Technol.* 4 (1988) 1072–1078.
- [15] Y. Shida, G.C. Wood, F.H. Stott, D.P. Whittle, B.D. Bastow, Intergranular oxidation and internal void formation in Ni-40% Cr alloys, *Corros. Sci.* 21 (1981) 581–597.
- [16] G.C. Wood, F.H. Stott, D.P. Whittle, Y. Shida, B.D. Bastow, The high temperature internal oxidation and intergranular oxidation of nickel-chromium alloys, *Corros. Sci.* 23 (1983) 9–25.
- [17] Y. Shida, F.H. Stott, B.D. Bastow, D.P. Whittle, G.C. Wood, Development of preferential intergranular oxides in nickel-aluminum alloys at high temperatures, *Oxid. Met.* 18 (1982) 93–113.
- [18] M.W. Brumm, H.J. Grabke, B. Wagemann, Oxidation of NiAl - III. Internal and intergranular oxidation, *Corros. Sci.* 36 (1994) 37–53.
- [19] C.S. Giggins, F.S. Pettit, Oxidation of Ni-Cr-Al alloys between 1000° and 1200°C, *J. Electrochem. Soc.* 118 (1971) 1782–1790.
- [20] F.H. Stott, G.C. Wood, Y. Shida, D.P. Whittle, B.D. Bastow, The development of internal and intergranular oxides in nickel-chromium-aluminum alloys at high temperature, *Corros. Sci.* 21 (1981) 599–624.
- [21] D. Oquab, N. Xu, D. Monceau, D.J. Young, Subsurface microstructural changes in a cast heat resisting alloy caused by high temperature corrosion, *Corros. Sci.* 52 (2010) 255–262.
- [22] C. Desgranges, F. Lequien, E. Aublant, M. Nastar, D. Monceau, Depletion and voids formation in the substrate during high temperature oxidation of Ni-Cr alloys, *Oxid. Met.* 79 (2013) 93–105.
- [23] T. Watanabe, An approach to grain-boundary design for strong and ductile polycrystals, *Res Mechanica* 11 (1984) 47–84.
- [24] H. Tézenas Du Montcel, L. Nazé, V. Maurel, N. Souai, R.E. Logé, J.Y. Guedou, Ingénierie des joints de grain dans les alliages à base de nickel, XIXème Congrès Français de Mécanique, (2009) Marseille, France, pp. 6.
- [25] V. Trindade, H.-J. Christ, U. Krupp, Grain-size effects on the high-temperature oxidation behaviour of chromium steels, *Oxid. Met.* 73 (2011) 551–563.
- [26] J.G. Goedjen, D.A. Shores, The effect of alloy grain size on the transient oxidation behavior of an alumina-forming alloy, *Oxid. Met.* 37 (1992) 125–142.
- [27] L. Li, X. Gong, X. Ye, J. Teng, Y. Nie, Y. Li, Q. Lei, Influence of Building Direction on the Oxidation Behavior of Inconel 718 Alloy Fabricated by Additive Manufacture of Electron Beam Melting, (2018).
- [28] P. Lin, G. Palumbo, U. Erb, K.T. Aust, Influence of grain boundary character distribution on sensitization and intergranular corrosion of alloy 600, *Scr. Metall. Mater.* 33 (1995) 1387–1392.
- [29] S. Yamaura, Y. Igarashi, S. Tsurekawa, T. Watanabe, Structure dependant intergranular oxidation in Ni-Fe polycrystalline alloy, *Acta Mater.* 47 (1999) 1175–1180.
- [30] S.-i. Yamaura, S. Tsurekawa, T. Watanabe, The control of oxidation-induced intergranular embrittlement by grain boundary engineering in rapidly solidified Ni-Fe alloy ribbons, *Mater. Trans.* 44 (2003) 1494–1502.
- [31] B. Pieraggi, Calculations of parabolic rate constants, *Oxid. Met.* 27 (1987) 177–185.
- [32] A. Chyrkin, P. Huczowski, V. Shemet, L. Singheiser, W.J. Quadackers, Sub-scale depletion and enrichment processes during high temperature oxidation of the nickel base alloy 625 in the temperature range 900–1000 degrees C, *Oxid. Met.* 75 (2011) 143–166.
- [33] V.S. Babu, A. Pavlovic, M.S. Seehra, Oxidation characteristics and thermal expansion of inconel alloy 718 from 300 K to 1273 K, *Superalloys 718 (625) (1997)* 689–693 706 and various derivatives.
- [34] A. Bennouna, Etude de l'oxydation du superalliage réfractaire inconel 718(NC19FeNb), Role Des Précipités De Carbure De Niobium Et De La Phase Delta (Ni3Nb), Institut National Polytechnique de Toulouse, 1986 PhD Thesis.
- [35] R. Rolland, Study of the Influence of the Steam Water on High Temperature Oxidation of Chromia Forming Nickel Based Superalloy, PhD thesis University of Blaise Pascal, Clermont-Ferrand II, 2012.
- [36] L.X. Zhou, T.N. Baker, Effects on dynamic and metadynamic recrystallization on microstructures of wrought IN-718 due to hot deformation, *Mater. Sci. Eng. A* 196 (1995) 89–95.
- [37] B. Pieraggi, R.A. Rapp, J.P. Hirth, Role of interface structure and interfacial defects in oxide scale growth, *Oxid. Met.* 44 (1995) 63–79.
- [38] D.J. Young, High Temperature Oxidation and Corrosion of Metals, Elsevier, Amsterdam, 2008.
- [39] F.I. Wei, F.H. Stott, The influence of aluminium on the oxidation of a Cr2O3-forming nickel-chromium alloy, *React. Solids* 6 (1988) 129–144.
- [40] F. Delaunay, C. Berthier, M. Lenglet, J.-M. Lameille, SEM-EDS and XPS studies of the high temperature oxidation behaviour of inconel 718, *Microchim. Acta* 132 (2000) 337–343.
- [41] V.B. Trindade, U. Krupp, P.E.G. Wagenhuber, H.J. Christ, Oxidation mechanisms of Cr-containing steels and Ni-base alloys at high-temperatures - Part I: the different role of alloy grain boundaries, *Mater. Corros. Und Korrosion* 56 (2005) 785–790.
- [42] S. Cruchley, H.E. Evans, M.P. Taylor, M.C. Hardy, S. Stekovic, Chromia layer growth on a Ni-based superalloy: sub-parabolic kinetics and the role of titanium, *Corros. Sci.* 75 (2013) 58–66.
- [43] C. Duhamel, J. Caballero, T. Couvant, J. Crépin, F. Gaslain, C. Guerre, H.-T. Le, M. Wehbi, Intergranular oxidation of nickel-base alloys: potentialities of focused ion beam tomography, *Oxid. Met.* 88 (2017) 447–457.
- [44] C. Juillet, A. Oudriss, J. Balmain, X. Feugas, F. Pedraza, Characterization and oxidation resistance of additive manufactured and forged IN718 Ni-based superalloys, *Corros. Sci.* (2018).
- [45] M. Calandri, D. Manfredi, F. Calignano, E.P. Ambrosio, S. Biamino, R. Lupoi, D. Ugues, Solution treatment study of inconel 718 produced by SLM additive technique in view of the oxidation resistance, *Adv. Eng. Mater.* 0 (2018).
- [46] A. Prillieux, E. Andrieu, Personal research, ENSIACET student project, "Intergranular Oxidation of Alloy 718 at 1050 °C", (2018).
- [47] A. Strondl, M. Palm, J. Gnauk, G. Frommeyer, Microstructure and mechanical properties of nickel based superalloy IN718 produced by rapid prototyping with electron beam melting (EBM), *Mater. Sci. Technol.* 27 (2011) 876–883.
- [48] Y. Idell, L.E. Levine, A.J. Allen, F. Zhang, C.E. Campbell, G.B. Olson, J. Gong, D.R. Snyder, H.Z. Deutchman, Unexpected d-Phase formation in additive-manufactured Ni-Based superalloy, the minerals, *Metals Mater. Soc.* 68 (2016) 950–959.
- [49] X. Wang, F. Fan, J.A. Szpunar, L. Zhang, Influence of grain orientation on the incipient oxidation behavior of Haynes 230 at 900°C, *Mater. Charact.* 107 (2015) 33–42.
- [50] A.P. Sutton, Grain-boundary structure, *Int. Met. Rev.* 29 (1984) 377–404.
- [51] S. Kobayashi, R. Kobayashi, T. Watanabe, Control of grain boundary connectivity based on fractal analysis for improvement of intergranular corrosion resistance in SUS316L austenitic stainless steel, *Acta Mater.* 102 (2016) 397–405.
- [52] U. Krupp, P.E.G. Wagenhuber, W.M. Kane, C.J. McMahon, Improving resistance to dynamic embrittlement and intergranular oxidation of nickel based superalloys by grain boundary engineering type processing, *Mater. Sci. Technol.* 21 (2005) 1247–1254.
- [53] W.R. Sun, S.R. Guo, J.H. Lee, N.K. Park, Y.S. Yoo, S.J. Choe, Z.Q. Hu, Effects of phosphorus on the δ-Ni3Nb phase precipitation and the stress rupture properties in alloy 718, *Mater. Sci. Eng. A* 247 (1998) 173–179.
- [54] M.S.A. Karunaratne, P. Carter, R.C. Reed, On the diffusion of aluminium and titanium in the Ni-RICH Ni-Al-Ti system between 900 and 1200°C, *Acta Mater.* 49 (2001) 861–875.
- [55] M. Hasaka, T. Morimura, Y. Uchiyama, S.-i. Kondo, T. Watanabe, K. Hisatsune, T. Furuse, Diffusion of copper, aluminum and boron in nickel, *Scr. Metall. Mater.* 29 (1993) 959–962.
- [56] A. Prillieux, Hydrogen and water vapour effects on oxygen solubility and diffusivity in high temperature Fe-Ni alloys, PhD Thesis, School of Materials Science and Engineering, University of New South Wales Sydney, 2017.
- [57] J. Askil, Tracer diffusion in the chromium-nickel system, *Phys. Status Solidi* 8 (1971) 587–596.
- [58] R.V. Patil, G.B. Kale, Chemical diffusion of niobium in nickel, *J. Nucl. Mater.* 230 (1996) 57–60.
- [59] R. Grieseler, I.S. Au, T. Kups, P. Schaaf, Diffusion in thin bilayer films during rapid thermal annealing, *Phys. Status Solidi* 211 (2014) 2635–2644.
- [60] S.V. Divinski, G. Reiglitz, G. Wilde, Grain boundary self-diffusion in polycrystalline nickel of different purity levels, *Acta Mater.* 58 (2010) 386–395.